



Spin-polarized electronic states and atomic reconstructions at antiperovskite Sr₃SnO(001) polar surfaces

Rémi Arras, J. Gosteau, D. Huang, H. Nakamura, H. J Zhao, C. Paillard, L. Bellaiche

► To cite this version:

Rémi Arras, J. Gosteau, D. Huang, H. Nakamura, H. J Zhao, et al.. Spin-polarized electronic states and atomic reconstructions at antiperovskite Sr₃SnO(001) polar surfaces. Physical Review B, 2021, 104 (4), 10.1103/PhysRevB.104.045411 . hal-03294503

HAL Id: hal-03294503

<https://hal.science/hal-03294503>

Submitted on 21 Jul 2021

HAL is a multi-disciplinary open access archive for the deposit and dissemination of scientific research documents, whether they are published or not. The documents may come from teaching and research institutions in France or abroad, or from public or private research centers.

L'archive ouverte pluridisciplinaire **HAL**, est destinée au dépôt et à la diffusion de documents scientifiques de niveau recherche, publiés ou non, émanant des établissements d'enseignement et de recherche français ou étrangers, des laboratoires publics ou privés.

1 Spin-polarized electronic states and atomic reconstructions at the antiperovskite 2 Sr₃SnO(001) polar surfaces

3 R. Arras,¹ J. Gosteau,¹ D. Huang,² H. Nakamura,³ H. J. Zhao,³ C. Paillard,⁴ and L. Bellaiche³

4 ¹*CEMES, Université de Toulouse, CNRS, UPS, 29 rue Jeanne Marvig, F-31055, Toulouse, France*

5 ²*Max Planck Institute for Solid State Research, 70569, Stuttgart, Germany*

6 ³*Physics Department and Institute for Nanoscience and Engineering University of Arkansas, Fayetteville, Arkansas 72701, USA*

7 ⁴*Laboratoire SPMS, CentraleSupélec/CNRS UMR8580,*

8 *Université Paris-Saclay, 8-10 rue Joliot-Curie, 91190 Gif-sur-Yvette, France*

We report a first-principles investigation of the atomic and electronic properties at the perfect and defective (001) surfaces of the antiperovskite Sr₃SnO. We first performed a thermodynamical study of the atomic structure terminations and demonstrated that SrSn-terminated surfaces should be the most stable one, either with a perfect (1 × 1) structure or with a (2 × 1) reconstruction induced by the formation of Sn vacancies. We detailed the surface gap states obtained for these surfaces, which we compare with those of other surface terminations, also having relatively low energies. These gap states, located near the Fermi level, could have a major contribution to the transport properties. Due to the lack of inversion symmetry associated with the surface, we predict that they also experience spin splittings, an important property for spinorbitronic applications. Finally, we found that Sr₂O-terminated surfaces could display a ferromagnetic ordering resulting from the population of 4d orbitals of Sr atoms at the surface and that this could lead to the formation of a spin-polarized two-dimensional electron gas.

I. INTRODUCTION

10 Antiperovskites, also known as inverse perovskites, possess the same crystallographic structure as normal
11 perovskites, but with cations and anions having inverted
12 their positions [1]. Following the fame of normal
13 perovskite compounds and the increased richness of their
14 interface and surface properties in nanostructures [2–4],
15 it is now considered that studying antiperovskites could
16 enable to enlarge again more the range of applications [5,
17 6] and of material candidates to display fundamental
18 quantum properties, such as superconductivity [7] or
19 topological electronic structures [8–10]. Understanding,
20 functionalizing and optimizing these properties in a new
21 class of materials requires extensive efforts to characterize
22 their heterostructures and to develop an engineering of
23 defects, surfaces and interfaces [11].

25 First-time grown in 1980 [12], Sr₃SnO is a good
26 example of an antiperovskite that shows good promises.
27 It has been predicted to be a 3D Dirac semimetal
28 with a band structure having 6 Dirac cones along
29 the Γ-X directions [13]. This material is formerly
30 classified as a topological crystalline insulator [14, 15],
31 that is, it displays surface states in the gap which
32 are preserved by crystal inversion symmetry [16], or
33 as a higher-order topological insulator displaying hinge
34 states [17]. Recently, a superconducting behavior below
35 a temperature $T \simeq 5$ K has been evidenced in Sr-
36 deficient Sr₃SnO antiperovskites [18–20] and some hints
37 of a ferromagnetic ordering have been attributed to the
38 possible presence of oxygen vacancies [21].

39 Sr₃SnO possesses a perovskite structure with Sn⁴⁺
40 and O²⁻ anions occupying respectively cuboctahedral
41 and octahedral atomic sites, formed by the sublattice of
42 Sr²⁺ cations [22]. The anionic nature of Sn elements
43 has been evidenced by Mössbauer spectroscopy in both

44 stoichiometric and Sr-deficient Sr₃SnO compounds [20].

45 It has also been confirmed by x-ray photoelectron
46 spectroscopy (XPS), while some signatures of neutral
47 or cationic Sn atoms near the surface were also
48 evidenced [22]. This finding can be related to the report
49 of possible closely-neutral Sn ions in the vicinity of a
50 Ca₃SnO surface [23].

51 The hypothetical [Sr²⁺]₃Sn⁴⁺O²⁻ compound would
52 display in consequences an alternation of (SrSn)²⁻
53 and (Sr₂O)²⁺ polar (001) atomic layers and a dipole
54 moment normal to the surfaces, thus corresponding to
55 surfaces of “type 3”, according to the classification
56 proposed by Tasker [24]. Conserving the bulk structure,
57 such a surface would be associated with the creation
58 of an internal electric field and to the divergence of
59 the electrostatic potential as a function of the film
60 thickness, unless a charge transfer of ±1 electron
61 per formula unit is transferred to the surface [25].

62 It can thus be expected that growing Sr₃SnO(001)
63 thin films could lead to electronic reconstructions, on
64 the basis of a polar catastrophe scenario [26, 27],
65 or atomic reconstructions with the stabilization of
66 structural defects such as vacancies. Due to the

67 particular structure of antiperovskites and its predicted
68 bulk band gap of a few tenths of meV, the properties
69 of Sr₃SnO are expected to be very sensitive to the
70 growth conditions and to its stoichiometry [20, 21].
71 Sr₃SnO and similar compounds have already been
72 grown epitaxially on different substrates such as yttria-
73 stabilized zirconia (YSZ)(001), LaAlO₃(001), or even
74 technologically-adapted substrates such as Si(001) using
75 a YSZ buffer layer [21, 22, 28, 29]. To our knowledge, only
76 (001)-oriented surfaces have been studied experimentally.

77 Concerning the theoretical studies on Sr₃SnO, most of
78 them have been performed by combining first-principles
79 calculations and tight-binding models in order to address

80 the topological nature of this material [14, 15, 17]. These
 81 works have however only considered ideal structures with
 82 perfect surfaces. More recently, the question of structural
 83 defects in the bulk crystal [30] and of perfect (001)
 84 surfaces [31] have been addressed separately and fully
 85 thanks to first-principles calculations.

86 To summarize, the surfaces of the antiperovskite
 87 Sr_3SnO , a candidate topological crystalline insulator,
 88 are polar surfaces for which the impact of possible
 89 electronic/chemical reconstructions on the protected
 90 surface states is not well understood. Those new
 91 surface structures could potentially lead to new ground
 92 states such as magnetic state, which has not previously
 93 been taken into account. Either conventional electronic
 94 reconstruction or magnetic transition could have a
 95 decisive effect on the true realization of surface states
 96 in these compounds. In consequence, we propose a
 97 detailed study based on *ab initio* calculations of the
 98 $\text{Sr}_3\text{SnO}(001)$ surfaces. We will first describe electronic
 99 reconstructions which appear at the perfect surfaces,
 100 with either a Sr_2O or a SrSn termination. The main
 101 properties of these surfaces will be compared with
 102 defective terminations in which vacancies or adatoms
 103 introduce atomic reconstructions and charge doping.
 104 A discussion of the relative stability of each surface
 105 termination is also provided.

II. CALCULATION DETAILS

107 We performed first-principles calculations based on
 108 the density functional theory (DFT) by using the
 109 Vienna *ab initio* software package (VASP) [32, 33].
 110 We employed the projector augmented wave (PAW)
 111 method [34], a cut-off energy of 550 eV and the
 112 generalized-gradient approximation of the exchange-
 113 correlation energy proposed by Perdew, Burke and
 114 Ernzerhof and revised for solids (GGA-PBESol) [35].

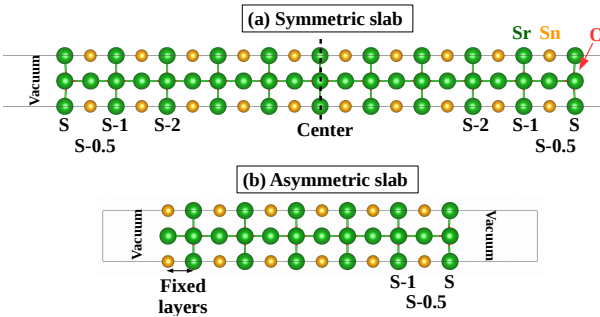


FIG. 1. (a) Symmetric and non-stoichiometric ($1 \times 1 \times 10.5$) slab with two non-equivalent Sr_2O -terminated surfaces and (b) Asymmetric and stoichiometric slab with a Sr_2O surface (S). The distance between the two atomic layers at the opposite surface is fixed to the bulk interplane distance.

115 As shown in Fig. 1, we performed direct calculations of
 116 the electronic properties of $\text{Sr}_3\text{SnO}(001)$ surfaces using

117 different slab geometries and including a vacuum layer
 118 with a thickness of at least 15 Å to separate the two
 119 surfaces. These slab calculations can be compared to the
 120 calculations of bulk properties described in Appendix A.
 121 The in-plane lattice parameters have been fixed to
 122 the calculated bulk equilibrium value of $a_0(\text{Sr}_3\text{SnO}) =$
 123 5.1 Å. Unless otherwise stated, the results presented in
 124 this paper have been obtained using more-convenient
 125 symmetric slabs, terminated by two equivalent surfaces
 126 and with a thickness of 21 atomic monolayers (MLs),
 127 that is 10 formula units (f.u.) of Sr_3SnO plus an added
 128 Sr_2O or SrSn ML (labeled 10.5 in the following). An
 129 example of such structure can be viewed in Fig. 1(a)
 130 for the case of a Sr_2O -terminated surface. Some
 131 differences obtained with such slab, if compared with an
 132 asymmetric slab, containing two non-equivalent surfaces
 133 [Fig. 1(b)], are also discussed throughout the paper, and
 134 more particularly detailed in Appendix B. We show in
 135 particular that, if the electronic reconstructions discussed
 136 in this paper have a different origin (off-stoichiometry or
 137 polar catastrophe) depending on the chosen geometry,
 138 they finally result in similar and robust surface states,
 139 with almost equal occupancy; only the symmetries induce
 140 noticeable changes, in the possibility that some bands
 141 will have to undergo spin-splitting lift of degeneracies.

142 The in-plane directions of the first Brillouin zone were
 143 sampled with a Monkhorst-Pack grid [36] of 15×15
 144 vectors, for a supercell with 1×1 lateral dimensions.

145 Bader charges have been calculated using the Bader
 146 charge analysis code described in Ref. [37].

147 In the following, the (S) and (S-0.5) denominations
 148 correspond respectively to the surface and subsurface
 149 atomic monolayers (MLs). The labels $[\text{Sr}]_{\text{O}}$ and $[\text{Sr}]_{\text{Sn}}$ are
 150 given for Sr atoms located in a $\text{Sr}_2\text{O}(001)$ or $\text{SrSn}(001)$
 151 ML.

III. UNRECONSTRUCTED (001) SURFACES

153 In this section, we will describe the atomic and
 154 electronic structure of unreconstructed (001) surfaces
 155 of Sr_3SnO . For the calculations, we used symmetric
 156 $1 \times 1 \times 10.5$ slabs terminated by two equivalent surfaces
 157 with the ideal Sr_2O or SrSn termination, as shown in
 158 Fig. 1(a).

A. $\text{Sr}_2\text{O}(001)$ -terminated surface

159 *a. Atomic structure:* At the Sr_2O -terminated
 160 surface, the interlayer distance is reduced to 2.43 Å
 161 between the surface (S) and subsurface (S-0.5) layers,
 162 *i.e.* by -4.7% if we compare with the bulk inter-atomic-
 163 layer distance of 2.55 Å. The calculated distortions
 164 then display oscillations in the following layers, with
 165 reduced magnitude (the interlayer distance is 2.59 Å
 166 (+1.4%) between the layers S-0.5 and S-1) up to the
 167 center of the slab, where we recover the bulk lattice

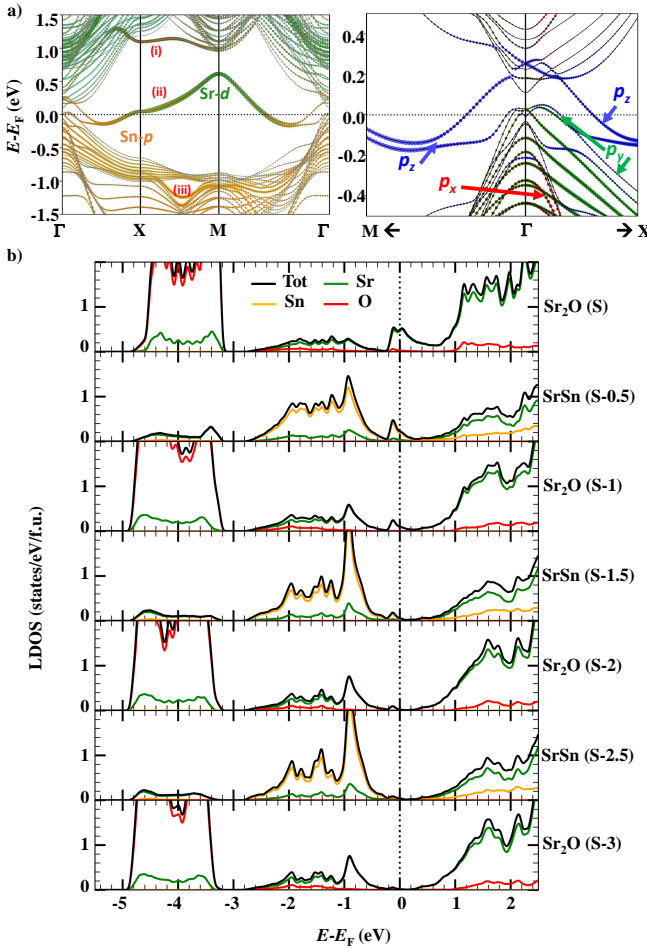


FIG. 2. (a) and structure calculated with a symmetric slab and nonmagnetic Sr₂O-terminated surfaces. The size of the colored circles is proportional to the contribution of each surface atom: On the left panel, the colors correspond to the [Sr]_O (green), O (red), [Sr]_{Sn} (cyan) and Sn (orange) atoms the nearest from the surfaces, while on the right panel, we display a zoom with the detailed of the surface Sn-*p* bands contributions around the Γ point. (b) Layer-resolved densities of states (LDOS).

parameter. Due to the different oxidation degree of each atom and the polar nature of Sr₃SnO, we also observe a cation-oxygen buckling along the $z[001]$ direction, which is $\Delta z = \langle z(\text{cation}) \rangle - \langle z(\text{anion}) \rangle = 0.173 \text{ \AA}$ at the surface layer. Such buckling is already 10 times smaller in the S-1 layer.

b. Electronic structure: The calculated band structure and the layer-resolved densities of states (LDOS) for the slab having a Sr₂O-terminated surface are given in Figs. 2(a) and 2(b). In the band structure, we can recover the bulk states forming parabolas centred around the Γ point, while the LDOS in atomic monolayers located in the center of the slab (starting from the layer (S-3)), are very similar to those of the bulk [see Fig. 11]. Clear gap states, labeled (ii) in the band structure, appear near the Fermi level. These gap states

are expected to primarily participate to the conduction and it can be noticed that their intensity decreases when going toward the center of the slab, to reach an almost 0 value at the layer (S-3). The integration of the total DOS between $E_F - 0.25 \text{ eV}$ and E_F is equal to 1.1 state, which will be occupied by electrons. Another surface state, labeled (i), can be observed around 1.2 eV above the Fermi energy, with a mix of [Sr]_O and O character, while lower Sn-*p* states (iii), also with a strong surface contribution can finally be noticed below $E_F - 1 \text{ eV}$.

The following observations are also made.

First of all, *p-d* band anticrossings, appearing along the Γ -X direction in the bulk band structure [see Appendix A], are now located above the Fermi level. In the bulk, these crossings happen at the intersection between Sr- $d_{y^2-z^2}$ and Sn- $p_y + ip_z$ (for X of coordinates (0.5,0,0)) and they are generally associated with pseudo-Dirac points [13, 38, 39]. In the vicinity of a surface, they cannot be Dirac points, as the inversion symmetry would not be preserved anymore; their band character is moreover slightly changed, as, because of the surface, the $y[010]$ and $z[001]$ directions are also not equivalent, which consequently induces a lift of degeneracy of the *p* states.

The second interesting point is that the bands (ii), forming the surface gap states near the Fermi level, display a different band character as a function of the considered wave vector \mathbf{k} : These bands have mainly a Sr(S)- d_{xz}, d_{yz} character between the $X(\frac{1}{2},0,0)$ and $M(\frac{1}{2},\frac{1}{2},0)$ points, a Sn(S-0.5)-*p_z* near the $\Gamma(0,0,0)$ point, and a mixed character otherwise. The two sets of bands corresponding to the surface states start changing their character around the $X/2$ and $M/2$ points, where these bands display a minimum. With this difference of orbital contributions, we also observe a different localization in real space. While these states between X and M are mostly unoccupied and possess a strong contribution coming from Sr atoms located in the surface layer (S), they tend to be more delocalized and they spread in the whole slab when having a Sn band character near the Γ point. This charge delocalization can be seen as a result of the *p_z* nature of the band and of the narrow band gap near Γ .

A third point is that, due to the position of the Fermi level, not only the aforementioned surface bands are crossing it, but also Sn-*p_y* bands, with a clear bulk nature, near the Γ point.

Finally, as it is shown in Appendix C, the band structure only slightly depends on the spin-orbit interaction, which only induces a small lift of degeneracy, splitting the surface states near the Fermi level into two sets of two non-spin-polarized bands around the X and M points.

c. Spin textures Still using a symmetric slab, we found out that, associated with the change of the orbital contributions of the surface states, we see a change of the spin orientation as a function of the wavevector \mathbf{k} : Always orientated in-plane, they are aligned along the

[010] direction between X/2 and X and along the [100] direction along the X-M direction. For the symmetric slab, no spin splitting was observed. On the contrary, using an asymmetric slab, which lacks the inversion symmetry, as a real surface would, we observe such spin splittings in the band structures, as shown in Fig. 3, which give spin textures consistent with a Rashba-like spin-orbit effect, with a dominant linear-in- \mathbf{k} term around the X and M points (with spin vectors tangent to the energy contour) and a non-negligible cubic character around the Γ point. The effective masses and splitting parameters calculated around the X and M points are given in Table II of Appendix B.

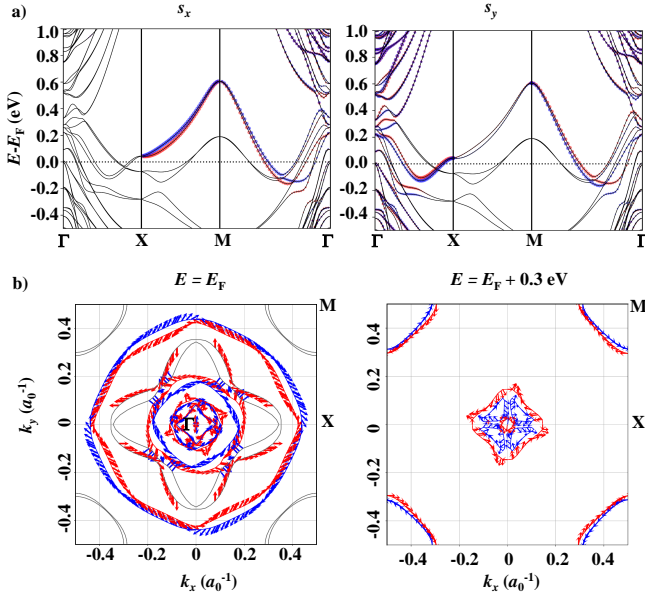


FIG. 3. Spin configurations at the Sr_2O -terminated surface as calculated with an asymmetric slab: (a) Spin-projected band structures and (b) iso-energy projections in the 2D 1st Brillouin zone, with the associated spin textures. Blue and red colors help to distinguish between the two splitted bands with opposite spin directions. Grey lines correspond to bands for which the atoms at the considered surface do not contribute.

d. Magnetic ordering: Up to now, we considered a perfect Sr_2O surface with the same nonmagnetic (NM) behavior as bulk Sr_3SnO compound. We also found it is possible to stabilize a ferromagnetic (FM) state, leading to the band structures shown in Figs 4(a) and 4(b); this FM state is more stable than the NM state, with an energy difference per surface f.u. $\Delta E = E_{\text{FM}} - E_{\text{NM}} = -0.43 \text{ meV } a_0^{-2}$. We would like to mention that it was only possible to calculate the above-mentioned magnetic state by adding the spin-orbit interaction. Using the asymmetric slab, even in the absence of the spin-orbit interaction, we were able to recover a similar magnetic state, with a difference of total energy per surface f.u. separating the FM and NM state of $\Delta E = -1.42 \text{ meV } a_0^{-2}$. From this observation, we can only infer the hypothesis that when the four surface bands, labeled

(ii), are fully degenerate, a NM state is more stable, while lifting some degeneracy (using an asymmetric slab or adding the spin-orbit interaction) implies that fully occupying one set of two-bands by one charge of a given spin is more favorable, inducing in consequence the emergence of a ferromagnetic ordering.

For the symmetric slab, the corresponding total magnetic moment is orientated along the [111] direction, while it is along the [001] direction with the asymmetric slab. In both cases, it has a magnitude of $0.84 \mu_B$ per surface f.u. The magnetic state appears to be a result of the charge reorganization, which results in the population of Sr-4d orbitals in the surface layer, as it can be seen in Figs 4(a) and Fig 4(c), in the case of a symmetric slab. The calculated total magnetic moment agrees with the redistribution of 2 electrons (one on each surface) resulting from the absence of a $(\text{SrSn})^{2-}$ layer. As it can be seen in Fig. 4(c), the Sr-4d orbitals are not strongly localized near the atom nucleus and the spin density strongly extends in the vacuum; it results that the calculated spin magnetic moment calculated from the integration of states projected in the atomic sphere centered on a surface Sr atom is only $0.05 \mu_B/\text{atom}$.

Concerning the band structure, due to the magnetic exchange interaction, the ferromagnetic ordering leads to a band spin splitting which is of approximately 0.8 eV for \mathbf{k} vectors for wavectors in the X-M direction, as it can be seen in Fig. 4(b). The band structure now displays bands crossing the Fermi level, which are linked to minority-spin electron pocket around the Γ point and to a majority-spin hole pocket around the M point.

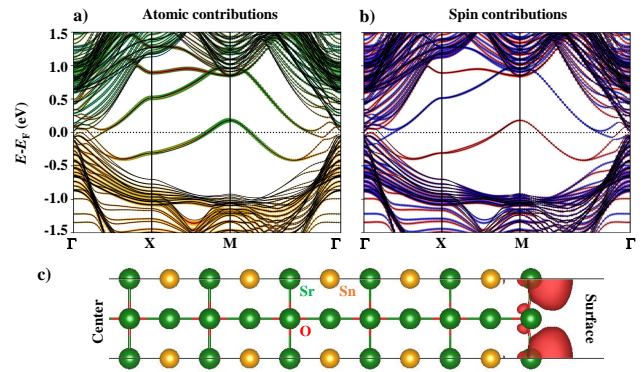


FIG. 4. Band structure of the perfect Sr_2O -terminated surface calculated with the spin-orbit interaction and for a magnetic state. a) The contribution of the atoms of the surface is given by the colored circles following the same color code than in Fig. 2. b) The sign of the spin projection s_z (with the quantization axis z along the [001] direction) on the band structure and c) the corresponding spin density is given in red for positive values and blue for negative values.

When the surfaces are in the FM states, the spin expectation values are orientated parallel to the total spin magnetic moment, *i.e.* along the [111] or [001] direction, respectively for the symmetric or

asymmetric slab, showing a dominance of the magnetic exchange interaction over the spin-orbit effects. With the asymmetric slab, small values of spin projections, reminiscent of the spin-orbit-induced spin textures, can be observed along the $x[100]$ and $y[010]$ directions only for bulk bands, that are near the Γ point or at energies below $E_F - 1$ eV.

314 B. SrSn(001)-terminated surface

315 *a. Atomic structure:* The interlayer distance 316 between the surface (S) and subsurface (S-0.5) 317 monolayer is calculated to 2.46 Å, which corresponds to 318 a reduction of -3.5% , that is lower than for the Sr₂O 319 termination, on the contrary to an almost two-times 320 larger cation-anion (Sr-Sn) buckling ($+0.39$ Å).

321 *b. Electronic structure:* Analyzing the electronic 322 structure of the SrSn-terminated surface [Fig. 5], we can 323 observe again the appearance of different surface gap 324 states. These gap states more precisely correspond to 325 depleting Sn- p states at the surface, which creates a band 326 bending and a shift of the bulk peak, originally located 327 at $E_F - 1$ eV, upward in energy, to the Fermi energy. 328 From the LDOS, we can thus observe a peak of high 329 density at the Fermi energy, resulting from bands with 330 low dispersion. Around the Γ point, we indeed observe 331 three sets of bands near the Fermi level, which correspond 332 to Sn- p surface states. One of these sets of bands, labeled 333 (i), stays close to the Fermi level and in the bulk band 334 gap away of Γ ; it possesses a majoritarily p_y character 335 in the Γ -X direction, with a low dispersion, while it 336 has a large p_z contribution along the directions X-M- 337 Γ . The second set of band, which is more dispersive 338 than the first one, possesses on the contrary a p_z , p_y 339 and $p_x + p_y$ character, respectively along the Γ -X, X-M 340 and M- Γ directions. The integration of the total DOS 341 between E_F and $E_F + 0.4$ eV indicates the formation of 342 0.9 holes per surface, distributed approximately over five 343 atomic layers.

344 Contrary to the NM Sr₂O surface for which the spin- 345 orbit interaction leads to almost no visible effects on 346 the electronic structure, it is important to note that for 347 this surface termination, the band gap between the set 348 of states (i) and (ii) at the X point is increased up to 349 0.2 eV as a direct result of the spin-orbit coupling. At 350 this high-symmetry point, we thus observe an avoiding 351 of the bands which is accompanied by a strong $p_y + p_z$ 352 hybridization. Finally, the third set of bands, labeled 353 (iii) and corresponding to Sn- p_x bands, displays a more 354 dispersive behavior with a minimum at $E_F - 1.5$ eV at the 355 X point. Both sets of bands (i) and (ii) cross the Fermi 356 level in the Γ -X and Γ -M directions, while the set (i), the 357 highest in energy and less occupied, displays a minimum 358 at the X point, and a maximum, corresponding to a hole 359 pocket at the M point, certainly resulting from the charge 360 reorganization induced by the nonstoichiometry of the 361 structure. In addition, it is also important to mention

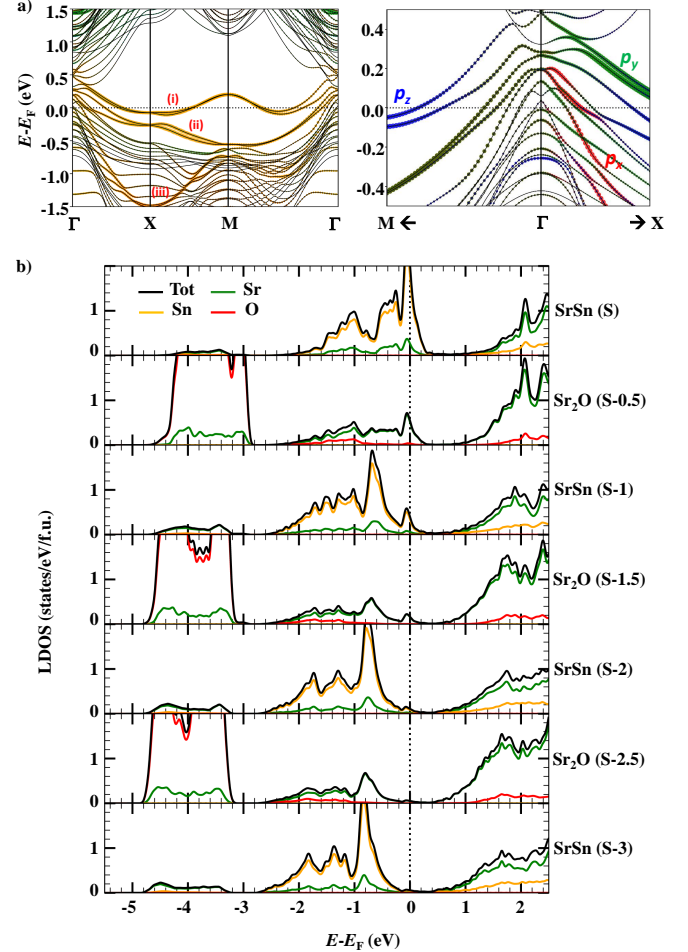


FIG. 5. (a) Band structure calculated for the SrSn-terminated surface. The size of the colored circles is proportional to the contribution of each surface atom: On the left panel, the colors correspond to the [Sr]_O (green), O (red), [Sr]Sn (cyan) and Sn (orange) atoms the nearest from the surfaces, while on the right panel, we display a zoom with the detailed of the surface Sn- p bands contributions around the Γ point. (b) Layer-resolved densities of states (LDOS).

362 that for this surface termination, we only predict the 363 appearance of an almost zero total spin magnetic moment 364 of $0.04 \mu_B$ per surface f.u. Using an asymmetric slab, 365 it is possible to stabilize a magnetic state, but its origin 366 certainly comes from the presence of the second and non- 367 physical surface (with the Sr₂O termination), which is 368 also primarily magnetized.

369 *c. Spin textures* As for the Sr₂O-terminated surface, 370 the spins at the SrSn surface are orientated in-plane 371 and along a direction perpendicular to the wavevector 372 \mathbf{k} . Using an asymmetric slab induces the appearance 373 of Rashba-like spin splittings, the values of which have 374 been calculated using the spin-projected band structures 375 of Fig. 6(a) and are given in Table II in Appendix B. 376 We can notice that these values are of the same order of 377 magnitude than for the other surface termination. Also

378 similarly to the Sr_2O surface, we can see from the spin
 379 textures presented in Fig. 6(b) again mostly a linear
 380 Rashba behavior related to tangential spins around the
 381 X and M points, while cubic contributions are expected
 382 to be responsible of the deviation from this behavior near
 383 the Γ point. Large increase of the spin splitting can be
 384 noticed on the spin textures, for wavevectors for which
 385 the bands (i) and (ii) are the closest one from each other.

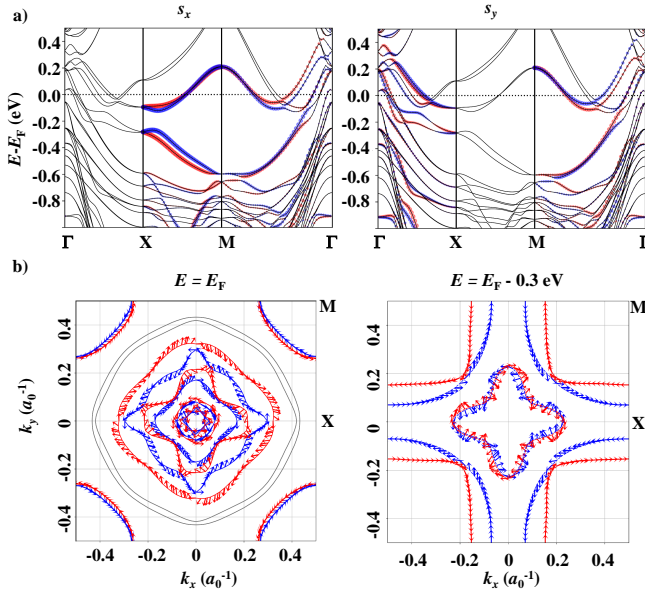


FIG. 6. Spin configurations at the SrSn-terminated surface as calculated with an asymmetric slab: (a) Spin-projected band structures and (b) Iso-energy projections in the 2D 1st Brillouin zone, with the associated spin textures. Blue and red colors help to distinguish between the two splitted bands with opposite spin directions. Grey lines correspond to bands for which the atoms at the considered surface do not contribute.

386 IV. RECONSTRUCTED (001) SURFACES

387 In the previous section, we considered perfect (001)
 388 surface terminations of Sr_3SnO , *i.e.* Sr_2O and SrSn, and
 389 we discussed the electronic modifications which appears
 390 in the vicinity of these surfaces. We will now verify
 391 which surface termination should be the most stable and
 392 if atomic reconstruction induced by the presence of point
 393 defects could be favored. When stable, we will describe
 394 the effects of these defects on the electronic and magnetic
 395 properties. The method to calculate the surface stability
 396 is explained in Appendix D. The properties described in
 397 this section have been calculated using $(2 \times 1 \times 10.5)$ slabs;
 398 as explained in Appendix D 3, as they were found more
 399 stable than $(\sqrt{2} \times \sqrt{2})\text{R}45^\circ$.

400 *a. Stability of the surface terminations:* The figure 7
 401 gives the phase diagram of the surface termination
 402 stability as a function of the variations of the chemical

403 potentials of Sr and Sn atoms. In a reasonable range of
 404 chemical potentials, we see that 5 different terminations
 405 can be stabilized. If we restrict ourselves to the chemical
 406 potentials fixed so that the bulk Sr_3SnO can be grown,
 407 we only have to consider the values matching with the
 408 dotted area in Fig. 7 [See Appendix D for more details];
 409 in that case, we can first conclude that, according to
 410 our calculations, there is in principle a higher probability
 411 to obtain a SrSn-terminated surface, with potentially
 412 Sn vacancies (V_{Sn}), leading ultimately to a $\text{Sr}_{\text{Sn}0.5}$
 413 surface (labeled " $\text{Sr}_{\text{Sn}} + \frac{1}{2}V_{\text{Sn}}$ "). The formation of Sr_2O -
 414 terminated surfaces, however, appear also realistic if we
 415 consider that their domain of stability are close to the
 416 limit of stability of the bulk and that our results may
 417 depend on the chosen exchange-correlation functional;
 418 in this latter case, we can see from Fig. 7 that the
 419 adsorption of oxygen atoms may lead to more stable
 420 $\text{Sr}_2\text{O}_{1.5}$ terminations (labeled " $\text{Sr}_2\text{O} + \frac{1}{2}\text{O}$ ") in oxygen-
 421 rich conditions.

422 To give a more quantitative idea of the energy
 423 differences between each surface termination, we can
 424 consider the averaged value of chemical potentials for
 425 which bulk Sr_3SnO is stable, *i.e.* the point of coordinates
 426 $\Delta\mu_{\text{Sr}} = -0.341 \text{ eV}$, $\Delta\mu_{\text{Sn}} = -1.440 \text{ eV}$, represented
 427 by a "+" sign in Figs. 7 and 15: With these values
 428 of chemical potentials, the energy difference between
 429 the perfect Sr_2O and SrSn terminated surfaces $\Delta\gamma_S =$
 430 $\gamma_{S=\text{Sr}_2\text{O}} - \gamma_{S=\text{SrSn}}$ is calculated to be almost 0 eV/surface
 431 formula unit and the calculated formation energy of a Sn
 432 vacancy at the SrSn surface is $E_d(V_{\text{Sn}}) = -0.21 \text{ eV}$ per
 433 defect [See Appendix D 3].

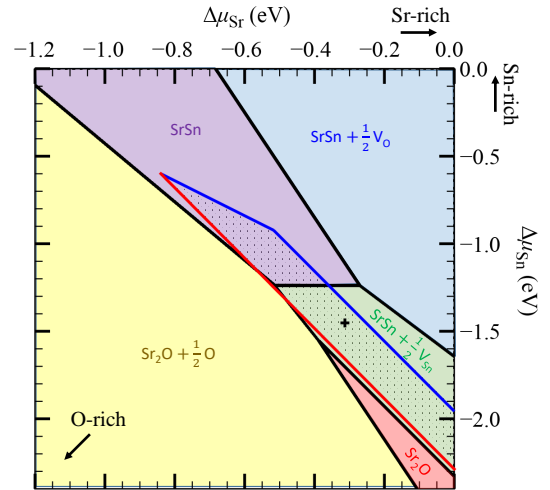


FIG. 7. Stability phase diagram for a $\text{Sr}_3\text{SnO}(001)$ surface. The dotted area corresponds to the domain of chemical potentials for which Sr_3SnO bulk can be synthetized [see Fig. 15 in Appendix D]. Each colored area corresponds to a chemical-potential domain for which a given surface termination is the most stable, *i.e.* displays the lowest surface energy γ_S as calculated using Eq. D5.

b. Induced atomic distortions: The introduction of a Sn vacancy at the SrSn-terminated surface does not change significantly the buckling, which is calculated to be 0.42 Å. Due to the unoccupied atomic sites created by the vacancy, we also observe an in-plane distortion, with a displacement of the surface Sr atoms away from the vacancy, by 0.38 Å along the x [100] direction. The buckling at the Sr₂O-terminated surface with an oxygen adatom is on the contrary strongly changed (-0.17 Å) with an inversion of its sign. The atomic structures calculated for these two defective surfaces are shown in the Appendix D 3 in Fig. 16.

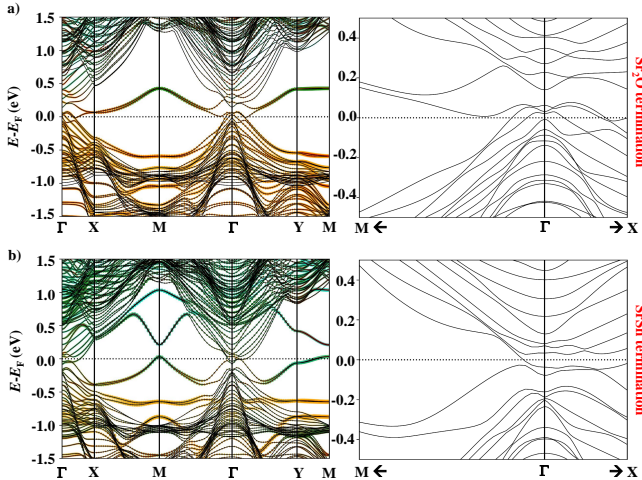


FIG. 8. Band structure of the most stable (2×1) defective surfaces, with (a) a Sr₂O_{1.5} (Sr₂O + $\frac{1}{2}$ O) termination or (b) a SrSn_{0.5} (SrSn + $\frac{1}{2}$ V_{Sn}) termination. The contributions of each atom of the surface are given by the colored circles following the same color code than in Fig. 2. A zoom of the band structures around the Γ point is given for each surface in the right panels.

c. Induced changes in the electronic structure: Figures 8(a) and 8(b) provide the band structures for the most stable (2×1) defective surfaces with respectively a Sr₂O_{1.5} and SrSn_{0.5} termination. The Sr₂O_{1.5}-terminated surface corresponds to a perfect (2×1) Sr₂O surface with an oxygen adatom located on top of one Sn atom. This surface displays a band structure very close to the one calculated for the perfect Sr₂O surface [Fig. 2(a)], except for the surface bands crossing the Fermi level for wavevectors closer from Γ in the Γ -Y and Γ -X directions, indicating that due to the presence of the additional negatively-charged oxygen ion, these bands tend to be less occupied. For this surface termination, it is also possible to note that the surface states near the Fermi level, which have mostly a Sn-*p* character for every surfaces, display a visible contribution from oxygen orbitals, as represented by the red circles.

If we now compare the defective SrSn_{0.5}-terminated surface [Fig. 8(b)] with its perfect counterpart [Fig. 5(a)], we can directly see that the surface states are strongly changed: This surface termination, certainly due to its

Sn deficiency, indeed seems *a priori* to present more similarities with the Sr₂O termination. We can in particular highlight the set of bands crossing the Fermi level at the M point, forming a small hole pocket with Sr-*d* character. It is also interesting to note that around the Γ point, the bottom of the bulk conduction bands are crossing the Fermi level. We only calculated a total magnetic moment of 0.002 μ_B , which is not significant.

V. BADER CHARGES AND CORE-LEVEL ENERGIES

Experimentally, the surface electronic structure of Sr₃SnO(001) has been investigated via ARPES [29] and XPS [22], both to map the band structure and to track the atomic valence states. Thus, in this section, we consider how the Bader charges and core-level energies (CLEs) are modified in perfect and reconstructed surfaces. These quantities are provided in Table I and will allow an analysis, complementary to the band structures described in Sections III and IV.

On the one hand, the formal oxidation states are obtained by subtracting calculated Bader charges to the number of electrons of the neutral Sr atom. Bader charge analysis [37] is one of the numerous methods which allow to obtain a numerical value of the charge carried by a chemical species [40] and this will help understanding the electronic reconstructions occurring in our systems. However, in practice, this method depends on a specific choice of partitioning of the real-space volume and particular care has to be taken when comparing Bader charges of bulk and surface atoms. We chose to restrict the use of this method to the analysis of charge occupancy on Sr atoms, which possess sufficiently localized *d* orbitals and for which we calculated significant variations.

On the other hand, the CLEs are also sensitive to the local chemical and electrostatic environment and can be probed experimentally by XPS. The binding energy E_b associated with the removal of a core electron can be measured directly and, in the so-called initial-state approximation [41–43], it is equal to the opposite of the CLE ε_c , referenced to the Fermi level E_F :

$$E_b = -\varepsilon_c = -(\epsilon_c - E_F) \quad (1)$$

In Fig. 9 and Table I, we provide the variation in the Sn-3d CLE across the different layers, referenced to the value in bulk Sr₃SnO, *i.e.* $\Delta\varepsilon_{Sn,3d} = \varepsilon_{Sn,3d}^{\text{layer}} - \varepsilon_{Sn,3d}^{\text{bulk}}$. Overall, the CLEs do not deviate by more than a few hundred meV from the value for anionic Sn in bulk Sr₃SnO, showing that anionic Sn remains stable and does not undergo a drastic change in valence state. Nevertheless, the small but systematic shifts in the Sn 3d CLEs across the different layers of the various slabs shed light on how charge is redistributed for the different surfaces. Similar to CLE shifts computed for surfaces of various transition metals [42], when small amounts of electrons (holes) are

TABLE I. Calculated properties of the $\text{Sr}_3\text{SnO}(001)$ surfaces: Surface and averaged core-level shifts $\Delta\varepsilon_{S_n,3d}$ and oxidation degrees estimated from the Bader charges for the Sr atoms in the surface layer. For a given defect, the calculated values are given for the structures with the lowest total energies [See Appendix D 3].

Structure	$\Delta\varepsilon_{S_n,3d}^S$ (eV)	$\langle \Delta\varepsilon_{S_n,3d} \rangle$ (eV)	$Q_{\text{Bader}}^S(\text{Sr})$ (e)
Bulk			
Perfect	-	0	+1.24
Sr_2O termination			
Perfect (NM)	0.011	0.072	+0.98
Perfect (FM)	-0.098	-0.015	+1.08
$+\frac{1}{2}\text{V}_{\text{Sr}}$	0.154	0.097	+1.28
$+\frac{1}{2}\text{V}_{\text{Sn}}$	-0.269	-0.182	+0.81
$+\frac{1}{2}\text{V}_{\text{O}}$	-0.095	-0.046	+0.69
$+\frac{1}{2}\text{O}$	0.165	0.100	+1.14
SrSn termination			
Perfect	0.338	0.205	+1.30
$+\frac{1}{2}\text{V}_{\text{Sr}}$	0.438	0.250	+1.31
$+\frac{1}{2}\text{V}_{\text{Sn}}$	0.120	-0.054	+1.15
$+\frac{1}{2}\text{V}_{\text{O}}$	0.307	0.137	+1.26

transferred to the Sn atoms, the extra potential rigidly shifts the valence DOS and core levels down (up) relative to the Fermi energy, thus increasing (decreasing) the CLE. We now describe the different surfaces in more details.

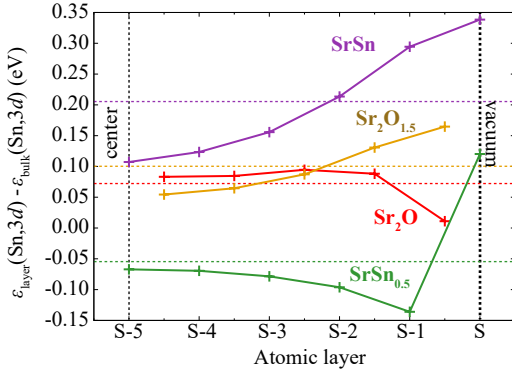


FIG. 9. Variation of the 3d core level energies $\varepsilon_{S_n,3d}$ as a function of the position of the Sn atom in regard to the surface layer (S). The colored dotted lines indicates the averaged CLE ($\langle \varepsilon_{S_n,3d} \rangle$).

Fisrt, we can consider the perfect Sr_2O surface. From the band structure given in Fig. 2(a), we saw the presence of a partially-occupied surface gap state with a mixed character associated with Sn-*p* and Sr-*d* orbitals. This observation is in agreement with the decrease of the oxydation degree by 0.26 e of the Sr atoms located at the surface, as compared with the bulk, *i.e.* with an increase of the number of electrons, which will populate

4*d* orbitals of these atoms. From Fig. 9, we can also notice a decrease of the CLE $\varepsilon_{S_n,3d}$, that is the appearance of a band bending and a local internal electric field between the atomic layers "S" and "S-1.5", also indicating a transfer of electron to the Sn-*p* orbitals. The CLE for Sn atoms close to the center of the slab are tending toward an averaged value 72 meV higher than the bulk CLE; this is consistent with the band structure of Fig. 2(a), in which we can see that bulk states are above the Fermi level, which is itself pinned by the surface states. When turning to a magnetic state, the Sn-3d CLE decrease by approximately 90 meV, mostly because of the lower lying partly-occupied surface state of majority spin.

Adding an oxygen atom at the (2×1) Sr_2O surface restores the bulk properties. It can indeed be seen that the calculated oxidation degree of the surface Sr atoms is +1.14 e, *i.e.* closer from the bulk value of +1.24 e. The averaged CLE, mostly representing bulk-like states, remains the same for this structure as for the perfect surface, while we can see an increase of the CLE for the subsurface atoms because of a shift of the Fermi level, which is consistent with a depopulation of the surface bands.

For the perfect SrSn termination, the charge balancing is obtained by distributing holes on Sn-*p* orbitals, which can be directly seen from the increase of the CLEs of the Sn atoms, while the oxidation degree of Sr atoms does not change significantly. Due to the less correlated nature of these bands, a part of these charges is localized near the surface, while the rest is spread over the whole slab. Because the SrSn surface is hole doped, while the Sr_2O surface is electron doped, we observe an internal electrical field which induces an opposite variation of the CLEs [See Fig. 9].

For the three surface terminations described up-to-now, we saw that the charge reconstructions are mostly involving surface atoms, and the CLEs in the center of the slab are converging toward similar values (between 70 and 100 meV). The situation is different when Sn vacancies are present at the SrSn -terminated surface: While the CLE of Sn atoms at the surface is of 0.12 eV, it is well lower for every other Sn atom (in particular Sn atoms in the (S-1) layer) and the CLEs of atoms in the center of the slab reach a value close to the average, *i.e.* -0.05 eV. The occupied *d* states at the M point observed in the band structure agree with the small diminution, by 0.1 e, of the Bader charge of the surface $[\text{Sr}]_{\text{Sn}}$ atom. This decrease is larger for the subsurface $[\text{Sr}]_{\text{O}}$ atoms: The oxidation degree is calculated to be +1.03 e, when averaged on all the 4 $[\text{Sr}]_{\text{O}}$ ions and it is -0.97 e if we consider only the two $[\text{Sr}]_{\text{O}}$ ions, first neighbors of the Sn vacancy.

To finish this analysis, we would like to point out that, ideally, $\Delta\varepsilon_{S_n,3d}$ should approach zero at the center of each slab, *i.e.* recover the bulk value. However, as we mentioned, there are differences ranging from 70 meV to 100 meV. The origin of these shifts is not easy to determine and it is difficult to rule out they can

591 originate from methodological artifacts, because of the
 592 choice of the slab geometry and its limited thickness, for
 593 example. An explanation for the lowest value (-50 meV),
 594 calculated for the $\text{SrSn}_{0.5}$ surface termination, will be
 595 given in the next section.

596 VI. DISCUSSION

597 *a. Stability of the surface terminations and atomic
 598 reconstructions:* In their first-principles study, Bilal
 599 *et al.* [31] already proposed, using another formalism,
 600 that a perfect $\text{SrSn}(001)$ -terminated surface of Sr_3SnO
 601 is energetically more stable than a Sr_2O -terminated one. The authors also suggested that due to the small
 602 energy difference, both terminations could be present in
 603 polycrystalline samples. Our calculations confirm this
 604 prediction. Among the possible contributions, which
 605 would help minimizing the surface energy, we can note
 606 that the SrSn termination allows a higher cation-anion
 607 buckling. Such buckling results in the creation of
 608 electric dipoles partially cancelling the internal electric
 609 field close to the surface, which is a consequence
 610 of the charge discontinuity associated with the polar
 611 nature of $\text{Sr}_3\text{SnO}(001)$. We also enlarged our study by
 612 considering the variations of chemical potentials, which
 613 can be related to experimental growth conditions, and by
 614 proposing simple surface reconstructions. We then found
 615 that a (2×1) $\text{SrSn}_{0.5}$ surface can be stable in Sn-poor
 616 conditions, which are still favorable to the growth of bulk
 617 Sr_3SnO . Finally, perfect or defectives Sr_2O -terminated
 618 surfaces could be obtained in oxygen-rich conditions.

619 Using the formula given in Ref. [22], it is possible
 620 to calculate core-level shifts (CLS) from the CLEs,
 621 which correspond, in this case, to the difference of
 622 binding energies between Sn-3d states in Sr_3SnO and
 623 in bulk α -Sn metal. For the $\text{Sr}_2\text{O}_{1.5}$ and $\text{SrSn}_{0.5}$
 624 surfaces, CLSs are in agreement with the CLSs measured
 625 by XPS: Reported experimental values are -1.10 eV
 626 and -1.05 eV, while calculated values for Sn atoms
 627 in the surface layer, are -1.12 eV and -1.07 eV,
 628 respectively. This tends to validate our model and
 629 suggests that these surface terminations may be present
 630 in their studied samples, which would be an interesting
 631 point to verify. The experimental finding of neutral
 632 Sn atoms near the surface [22, 23] may indicate that
 633 other possible reconstructions could be present, leading
 634 to the formation of other compounds than the Sr_3SnO
 635 antiperovskite, like metallic Sn clusters.

636 *b. Electronic reconstructions:* Considering the four
 637 most probable surface terminations, *i.e.* Sr_2O , $\text{Sr}_2\text{O}_{1.5}$,
 638 SrSn and $\text{SrSn}_{0.5}$, we can now discuss the electronic
 639 reconstructions, associated with charge transfer and
 640 redistribution or to the presence of point defects. For the
 641 perfect surfaces, because we used an electrically-neutral
 642 and nonstoichiometric structure with two equivalent
 643 surfaces, either with a Sr_2O or a SrSn termination,
 644 respectively two electrons or holes are expected to be
 645

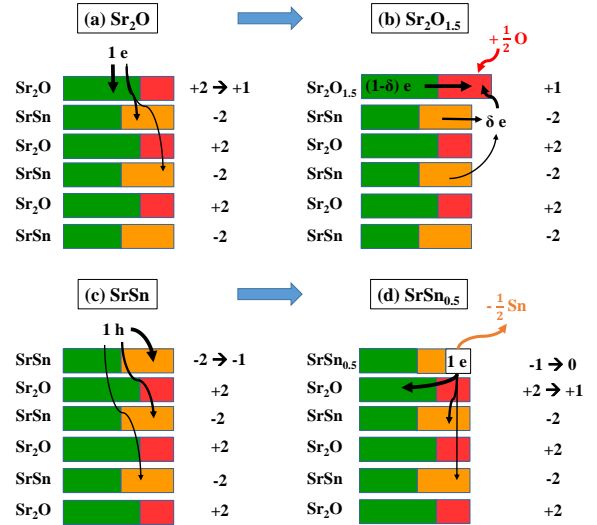


FIG. 10. Proposed diagrams showing the charge reconstruction at the four perfect or defective surfaces. The thickness of the arrows is approximately related to the amount of charges (electrons ("e") or holes ("h")) involved in the reorganization. The formal electric charges given on the right side of each atomic layers are approximated values before and after the electronic reconstruction (neglecting the charge extension away from the surface). The electronic reconstruction at the defective surfaces (b) and (d) may be explained relatively to the perfect surfaces (a) and (c). Green, orange and red squares represents the amount of Sr, Sn and O atoms. It is assumed that we consider a symmetric slab. Only a limited number of layers of a half of the slab is shown for the sake of simplicity.

646 re-distributed inside the structure and to either spread
 647 in the entire slab by populating bulk bands, or to be
 648 equally localized at the two surfaces, leading to $(\text{Sr}_2\text{O})^+$
 649 or $(\text{SrSn})^-$ terminations, this in order to preserve the
 650 electrical neutrality. A different mechanism involving
 651 charge transfer between the two different surfaces would
 652 settle if we used an asymmetric slab instead, but
 653 equivalent results are obtained for the perfect surfaces,
 654 as discussed in Appendix B.

655 For each surface, the main conclusions are summarized
 656 in Fig. 10 and explained below:

- 657 1. In the case of the electron-doped Sr_2O -terminated
 658 surfaces, an extra electron per f.u. is partly
 659 localized at the surface and will mostly populate
 660 the partially-occupied gap states, as it can be seen
 661 in the DOS and band structures of Fig. 2. These
 662 surface bands have mostly a contribution coming
 663 from 4d orbitals of Sr atoms, as witnessed by the
 664 lower oxidation degree, but also of p orbitals of
 665 Sn atoms in further atomic layers. The electron
 666 localization in surface Sr-4d orbitals can lead to
 667 the stabilization of a magnetic state, with a total
 668 spin magnetic moment of $0.84 \mu_B$ /surface f.u. As
 669 proposed in Fig. 10(a), in first approximation, that

is, if we omit partial charges occupying some bulk Sn-*p* bands, the localization of the extra electron would then turn the $[\text{Sr}_2\text{O}]^{2+}$ surface layer into $[\text{Sr}_2\text{O}]^+$. The electron doping can originate from the off-stoichiometric structure or from a charge balancing between the polar surface and a second surface or an interface [See Appendix B]. This interesting feature could enable to generate spin-polarized two-dimensional electron gases (2DEG), owing to the relatively low effective masses we calculated [See Table II in Appendix B].

2. The $\text{Sr}_2\text{O}_{1.5}$ surface, in which an oxygen adatom is introduced, is energetically favorable for samples grown in oxygen-rich environment. This extra oxygen atom will transform into a negatively-charged O^{2-} ion by attracting two electrons. Such scenario may provide another way to preserve the electric neutrality and, in the same time, to add one electron per f.u. to the surface, without inducing charge transfer to the 4*d* bands of Sr atoms [See Fig. 10(b)]. This statement is confirmed by the Bader charge, which stays close to the one calculated for the bulk compound and also by the band structure which displays less occupied surface states. As it can be seen on the 3*d* CLE variation displayed in Fig. 9, a part of the charge attracted by the oxygen atom to form the O^{2-} anion is taken from the Sn bands, which are thus moving upward in energy. Surface bands of Sn-*p* orbital character also display an hybridization with the oxygen adatom orbitals, this one being located on top of one of the Sn atom from the subsurface layer.
3. The SrSn surface possesses a band structure with a hole pocket around the M point (with a strong contribution from Sn atoms at the surface layer), as shown in Fig. 5. The variations of CLEs show, however, that a part of the charge redistribution also affects Sn-*p* states deeper in the slab. This process is summarized in Fig. 10(c). Again if we make the omission of the extension of the surface state away from the surface, we can then conclude that the $[\text{SrSn}]^{2-}$ surface is hole-doped and turned into a $[\text{SrSn}]^-$ surface. According to our calculations, such surface could then host a quasi-two-dimensional hole gas (q2DHG).
4. Concerning the Sn-deficient $\text{SrSn}_{0.5}$ surface, the counting of the total formal charges leads to the conclusion that with the proposed symmetric slab geometry, we expect to have a redistribution of 1 electron per surface f.u., as for the perfect Sr_2O termination. The band structure in Fig. 8(b) shows indeed that one surface gap state is almost completely filled, suggesting some charge localization near the surface, with a mixed Sn-*p* and $[\text{Sr}]_{\text{O}-d}$ character, as a function of the considered wavevector. First, it is important to note that the

occupied Sr orbitals are those of Sr atoms of the subsurface layer (S-0.5) and not of the surface layer (S). The electronic reconstruction indeed does not involve the surface atomic layer, which is predicted to be electrically neutral, in agreement with the calculated value of the CLE of surface Sn ions (which is close from the averaged values calculated for the other surfaces). The band structure also shows that the bottom of the bulk conduction bands is crossing the Fermi level, inducing a total closure of the band gap at the Γ point, which would indicate that the remaining electron is transferred to the bulk. This occupation of bulk states is consistent with the calculated Sn CLEs in the center of the slab, which tends to a lower value in the center of the slab than the three other surfaces. In this scenario, both bulk and surface states are expected to participate to transport properties. As shown in Fig. 10(d), we thus propose a scenario in which the Sn vacancies at the surface are transferring charges mostly to the first-neighbor Sr_2O layer, but also partly to other inner layers.

To summarize, we proposed 4 different surfaces, 2 being hole-doped (with SrSn and $\text{Sr}_2\text{O}_{1.5}$ terminations) and the 2 others being electron-doped. For every interface, we observed clear surface states in the band gap of Sr_3SnO and which cross the Fermi level. These bands tend to spread away from the surface for wavevectors close to the Γ points, while they are associated with carriers more confined in the surface layer for wavevectors near the X and M points, in particular when they involve 4*d* orbitals. The characterization of such surface states as topological states would require a deeper analysis, which is beyond the scope of the present paper. We can however notice that the calculated states are crossing the Fermi level and are joining the bulk valence and conduction bands near the Γ point, as expected for topological states. These states may also look like projected states calculated with a DFT+tight-binding method by Chiu, *et al.* [15], who also predicted the possibility that such states would experience spin splittings. Finally, we showed that these lifts of degeneracies require the presence of the spin-orbit interaction, which is not the case for these surface states to exist, a property which has also been demonstrated in the case of topological crystalline insulators [16].

c. Magnetic state: An important point in our results is that we demonstrated that the 2DEG could be spin polarized, with the formation of a FM ordering. The stabilization of such magnetic ordering is consistent with earlier theoretical report of a magnetic state in Sn-deficient bulk Sr_3SnO [See Ref. [30] and Appendix D 3]; indeed, our symmetric slab with two equivalent Sr_2O surfaces also corresponds to a Sn-deficient structure with one missing $\text{SrSn}(001)$ atomic layer. However, it is not probable that such ordering would remain at room temperature. It seems moreover clear from our calculations that it is not robust versus the presence of

784 atomic defects or any change of the surface termination.
 785 More surprisingly, the $\text{SrSn}_{0.5}$ surface is also found to
 786 be nonmagnetic, while containing Sn vacancies, which
 787 may indicate a more complex physics, related with
 788 the fact that occupied Sr-*d* bands are located in the
 789 subsurface layer and not at the surface. Sr_3SnO is not
 790 the first d^0 oxides which would exhibit ferromagnetism,
 791 as other examples have been studied and the subject
 792 of debate for several years now. We can first cite
 793 the example of the famous $\text{LaAlO}_3/\text{SrTiO}_3$, in which a
 794 ferromagnetic state has first been evidenced in 2007 [44].

795 Some studies have suggested that it may result from
 796 the presence of localized 3*d* gap states induced by the
 797 presence of defects [45, 46]. If the exact origin of
 798 the magnetic ordering at this interface is subject to
 799 debate, it has been noticed both the TiO_2 and SrO
 800 interface terminations can display ferromagnetism [47].
 801 The physics of magnetic d^0 systems has often been
 802 compared with the establishment of ferromagnetism in
 803 diluted ferromagnetic semiconductors (DMS). Induced
 804 ferromagnetic ordering has been already reported or
 805 predicted in other dopant-free (*i.e.* without the addition
 806 of impurities) bulk materials such as TiO_2 , SrTiO_3
 807 or ZnO [48, 49], but also in compounds presenting
 808 less localized unoccupied 4*d* or 5*d* orbitals, such as α -
 809 PbO , In_2O_3 , SnO_2 , ZrO_2 or HfO_2 [49–56]: In general,
 810 the magnetic ordering is obtained by either changing
 811 the stoichiometry, by adding interstitials or vacancies,
 812 and/or by considering surfaces or confinement effects;
 813 while electron-doped materials result in partially filled
 814 *d* orbitals, filling oxygen *p* orbitals with holes may also
 815 induce ferromagnetism [50, 57]. The case of oxygen-
 816 deficient ZrO_2 is particularly interesting, as it has been
 817 shown that the ferromagnetic ordering was more likely to
 818 form in thin films or nanoparticles. Albanese, *et al.* [55]
 819 demonstrated that in nanoparticles the magnetic state
 820 only forms if the number of low-coordinated Zr atoms is
 821 sufficient in regard to the number of excess and available
 822 charges. They also found that the ferromagnetic ordering
 823 is favored by the hybridization between the gap states
 824 and the bands at the bottom of the conduction bands.
 825 Applied to our system, such explanation could match
 826 with our observations.

827 *d. Other surfaces:* Finally, even if other surface
 828 terminations are predicted to be less stable, we cannot
 829 discard that they could be obtained. It is important
 830 to keep in mind that growth mechanisms rely on
 831 out-of-equilibrium processes and that our calculated
 832 results are given for a specific exchange-correlation-
 833 energy functional. In addition, post-treatment like
 834 chemical treatments or post-annealing could be used
 835 to select a specific termination. In particular, we
 836 can mention the surface with a *SrSn* termination and
 837 an oxygen vacancy in the subsurface layer, which
 838 could be grown in oxygen-poor conditions, or the
 839 $\text{Sr}_{1.5}\text{O}$ termination, which possess *Sr* vacancies with
 840 a relatively low formation energy [See Table IV] and
 841 calculated CLSs ($\simeq -1.05$ eV) which also match with

842 the above-mentioned experimental measurements [22].
 843 Sr vacancies are particularly interesting because they
 844 are associated with the emergence of a superconductive
 845 behavior for a temperature below 5 K and resulting from
 846 hole doping. In their study, Oudah, *et al.* [18], proposed
 847 that Cooper pairs could have either a pure *p*-*p* orbital
 848 character or a mixed *p*-*d* character. According to our
 849 calculations, at least in the vicinity of a Sr-deficient
 850 surface, we expect the bands crossing the Fermi level
 851 and being doped by holes, to possess mostly a pure *p*
 852 character.

VII. CONCLUSION

854 To summarize, we performed a study, as complete as
 855 possible, of the $\text{Sr}_3\text{SnO}(001)$ surface states. We identified
 856 different surface terminations, which could be stable
 857 depending on the growth conditions, and we predict that
 858 SrSn-terminated surfaces are more likely to be obtained
 859 using suitable conditions for the growth of the Sr_3SnO
 860 antiperovskite.

861 We detailed the electronic properties of four
 862 terminations, which are the perfect Sr_2O and SrSn
 863 terminations and the (2×1) reconstructed $\text{Sr}_2\text{O}_{1.5}$ and
 864 $\text{SrSn}_{0.5}$ surfaces. Each surface displays clear gap states
 865 with a strong surface contribution around the X and
 866 M wavevectors, indicative of a two-dimensional carrier
 867 localization, which could lead to the emergence of a two-
 868 dimensional system. We found that electronic or atomic
 869 reconstruction favoring electron transfer to the surface
 870 induce the presence of mixed Sn-*p* and Sr-*d* states, while
 871 hole transfer implies that only pure *p* states will cross the
 872 Fermi level.

873 Finally, we found that in the case of a perfect Sr_2O
 874 termination, the surface could host a ferromagnetic
 875 ordering, due to the occupation of the Sr-4*d* orbitals.
 876 This ordering is however not expected to be robust as
 877 we have shown that it can be destroyed by the addition
 878 of defects. On the contrary, the lack of spatial inversion
 879 symmetry induced by the surface, is suitable to the
 880 appearance of Rashba-like spin splittings, which could be
 881 another interesting feature of this interface, as it could
 882 be used in applications based on spin-to-charge current
 883 conversions.

ACKNOWLEDGMENTS

884

885 This study has been partially supported through
 886 the EUR Grant NanoX No. ANR-17-EURE-0009 in
 887 the framework of the *Programme des Investissements*
 888 *d’Avenir*. H.J., C.P. and L.B. thank the Vannevar
 889 Bush Faculty Fellowship (VBFF) from the Department
 890 of Defense. This work was granted access to the
 891 HPC resources of CALMIP (Allocation No. 2020-
 892 2021/P1229).

893

Appendix A: Bulk calculations

894 The calculated equilibrium lattice parameter of the
 895 cubic bulk Sr_3SnO is $a_0(\text{Sr}_3\text{SnO}) = 5.10 \text{ \AA}$, *i.e.* -0.4%
 896 lower than the experimental parameter of 5.12 \AA [12].
 897 If the spin-orbit interaction is switched-off, the band
 898 structure of bulk Sr_3SnO shows that a band with a
 899 $\text{Sn}-p_y + ip_z$ character crosses the Fermi level in the Γ -
 900 X, Γ -M and Γ -R directions. As reported in Ref. [13]
 901 and shown in Fig. 11, when including the spin-orbit
 902 interaction, the band structure is gapped in the Γ -M and
 903 Γ -R directions and only two bands (omitting the spin
 904 degeneracy), with $\text{Sn}-p_y + ip_z$ and $\text{Sr}-d_{y^2-z^2}$ characters,
 905 are forming an anticrossing at the Fermi level in the Γ -X
 906 direction forming a pseudo-Dirac point. This anticrossing
 907 is characterized by the presence of a small band gap of 7
 908 meV.

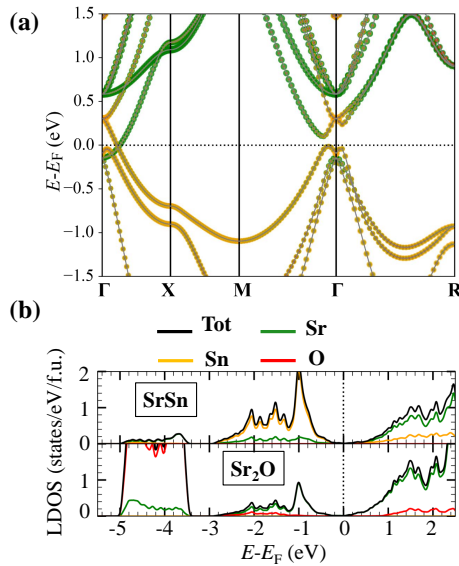


FIG. 11. Electronic structure of bulk Sr_3SnO calculated with the PBESol functional and the spin-orbit interaction: (a) Band structure for which the high-symmetry points have the coordinates $\Gamma(0,0,0)$, $X(\frac{1}{2},0,0)$, $M(\frac{1}{2},\frac{1}{2},0)$ and $R(\frac{1}{2},\frac{1}{2},\frac{1}{2})$, (b) LDOS. The contribution of each atom are highlighted with colors.

909 We also tested the influence of the exchange-
 910 correlation functional on the bulk electronic properties
 911 of Sr_3SnO . In Ref. [58], Vidal, *et al.*, warned that using
 912 standard DFT functional could lead to false positive
 913 predictions of topological nature of some materials
 914 because of the underestimation of the band gap and the
 915 wrong determination of the relative energies between p
 916 and d bands. For this reason, we performed, for the
 917 bulk structure only, calculations using computationally
 918 more-demanding functionals. In the Γ -M direction, using
 919 the PBESol functional, we calculated a band gap width
 920 equal to 39 meV at the d - p antricrossing. We found
 921 that the semi-metallic character is preserved with other
 922 functionals, but the band gap is increased to 159 meV

923 with the SCAN functional [59], and to 122 meV or
 924 146 meV, using a PBESol+ U [60] functional, with the
 925 U -dependent correction applied on the $4d$ bands of Sr
 926 atoms and $U = 1 \text{ eV}$ or $U = 2 \text{ eV}$, respectively. Finally,
 927 when using the hybrid functional HSE06 [61], the band
 928 crossing is shifted toward the Γ point, which results in a
 929 closing of the band gap at this same point, this results is
 930 in agreement with the calculations reported in Ref. [14].
 931 Unfortunately, the use of such functional is too time
 932 consuming to proceed to a more general comparison with
 933 surface calculations.

934 Appendix B: Dependence on the choice of the slab 935 geometry

936 As explained in Section II, we proposed to describe
 937 mostly our results issued from calculations performed
 938 with a symmetric slab, *i.e.* formed with two
 939 equivalent surfaces. By construction, such a slab is
 940 non-stoichiometric, which may have consequences in
 941 particular for the study of polar materials. On the
 942 contrary, such geometry has the advantage to be able
 943 to consider only one interface at a time, which is
 944 convenient to compare the relative surface stabilities, but
 945 also to avoid artifactual atomic relaxations or charge
 946 transfers from a second interface, which is present
 947 using asymmetric slabs [See also the discussions in the
 948 supplemental material of Ref. [62]]. In this section,
 949 we will describe the main differences which can be
 950 expected regarding the choice of the geometry. To do
 951 so, in addition to the $(1 \times 1 \times 10.5)$ symmetric slab, we
 952 performed calculations using an asymmetric slab. The
 953 thickness of the new slab is of 6 layers of Sr_3SnO (12
 954 atomic monolayers) along the $z[001]$ direction. When
 955 optimizing the atomic structure, we fixed the positions
 956 of the atoms located in the two monolayers the nearest
 957 from one interface and let the positions of all other atoms
 958 relax.

959 By approximating the antiperovskite Sr_3SnO as a
 960 fully-ionic compound formed of Sr^{2+} cations and O^{2-}
 961 and Sn^{4-} anions, we expect the (001) layer to be
 962 polar and constituted of an alternation of $(\text{Sr}_2\text{O})^{2+}$ and
 963 $(\text{SrSn})^{2-}$ atomic layers. For an asymmetric film, with
 964 the combination of a SrSn and a Sr_2O surfaces, the
 965 polar character of Sr_3SnO leads to the appearance of an
 966 internal electric field for a thin film and an electronic
 967 reconstruction above a critical thickness following a
 968 polar catastrophe scenario, similarly to the processes
 969 proposed for polar-oxide-based heterostructures like the
 970 $\text{LaAlO}_3/\text{SrTiO}_3(001)$ interface [26, 27]: Above a certain
 971 thickness, because of the electric-potential build-up
 972 associated with the internal electric field, the bottom of
 973 the conduction band and the top of the valence band, at
 974 each thin-film extremity, cross the Fermi level, causing a
 975 Zener breakdown, *i.e.* a charge balancing by tunnelling
 976 of electrons from the p-type to the n-type surface. This
 977 charge transfer is in particular necessary to avoid the

divergence of the potential build-up as a function of the layer thickness. For Sr_3SnO , we can expect the transfer of 1 electron per formula unit (f.u.) from the $[\text{SrSn}]^{2-}$ to the $[\text{Sr}_2\text{O}]^{2+}$ surface, in order to cancel the potential build-up divergence; the band gap of Sr_3SnO being very low, the electronic reconstruction would be present for the lowest thickness.

In addition to the electronic reconstructions, other mechanisms have been proposed to explain the insulator-to-metal transition at polar interfaces, such as atomic reconstructions involving the formation of structural defects [46]. In the case of a symmetric slab, no internal electric field can appear between the two equivalent surfaces but the total atomic structure being non stoichiometric, the excess of positive or negative charges carried by the additional $[\text{Sr}_2\text{O}]^{2+}$ or $[\text{SrSn}]^{2-}$ atomic layer directly triggers the electronic reconstruction by redistributing the excess of positive or negative charges. This process would create surfaces carrying less, but non zero, electric charges, $[\text{Sr}_2\text{O}]^+$ or $[\text{SrSn}]^-$.

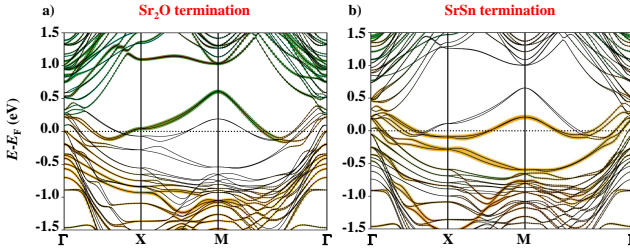


FIG. 12. Band structure calculated with the spin-orbit interaction for the (a) Sr_2O -terminated and (b) SrSn -terminated surface. The same color code is applied as in Fig. 2. When comparing with the band structure of Fig. 2 and 5, we can see that additional bands appear, which are the result of the presence of the second, non-equivalent and non-physical, surface, for which the atomic layers are fixed to the bulk positions.

The mechanisms explaining the calculated charge redistribution are then different depending on the slab geometries, but the charge redistribution can be nonetheless comparable for both configurations. As it can be seen by comparing Figs. 2(a) and 12(a) or Figs. 5(a) and 12(b), the band structures calculated for both geometries appear indeed similar; the crossing of the gap states with the Fermi level happens at almost the same values of wavevector for both structures and the band dispersions look similar, which suggests that like spin splittings in the band structure. Looking at an almost equal amount of charges is localized near the surface, independently of the chosen structure. This is confirmed by the Bader charges calculated for the Sr atoms located at the Sr_2O or SrSn -terminated surface, shown in Figs. 3 and 6. We can see from these figures which are respectively 1.00 e or 1.26 e, in the asymmetric slabs. The CLE $\varepsilon_{S_n,3d}^S$ is also almost the same for both slabs at the surface, that is respectively 0.17 eV and 0.14 eV, while the average over the whole slab differs because of the second surface, which induces the presence of a residual internal electric field, as it can be seen in Fig. 13. The values of these internal electric fields in Fig. 13. The values of these internal electric fields $E_{\text{field}} = \frac{\delta\varepsilon_{S_n,3d}}{\delta z}$, obtained by fitting the variation of CLE in the center of the slab, are $-11 \text{ meV } \text{\AA}^{-1}$ and $+16 \text{ meV } \text{\AA}^{-1}$, respectively for the Sr_2O - and SrSn -terminated interfaces.

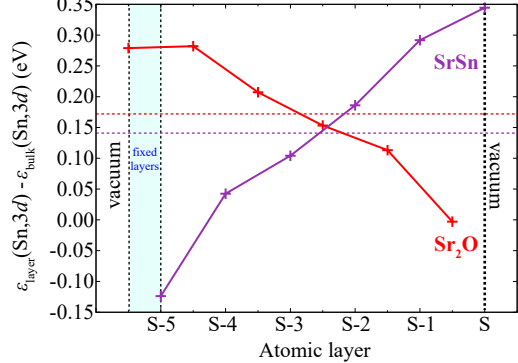


FIG. 13. Variation of the 3d core level energies $\varepsilon_{S_n,3d}$ as a function of the position of the Sn atom in regard to the surface layer (S). The colored dotted lines indicates the averaged CLE ($\langle \varepsilon_{S_n,3d} \rangle$). These results have been calculated using asymmetric slabs; they can be directly compared with those obtained with symmetric slabs and displayed in Fig. 9.

Beside the difference of stoichiometry, another question has to be addressed: It concerns the symmetries of our structures, in regard to the choice of slab geometry. This point is particularly important when considering spin-orbit effects. The bulk cubic perovskite structure possesses a $Pm\bar{3}m$ (No 221) space group associated with a O_h point group. When building the symmetric slab, the space group changes to $P4/mmm$ (No 123), with the fourfold rotation axis parallel to the normal to the (001) surface. Including a point defect on both surfaces with $(\sqrt{2} \times \sqrt{2})$ dimensions [see Appendix D 3], does not change the space group, while using (2×1) dimensions makes $x[100]$ and $y[010]$ directions to become non-equivalent and reduces the space group to $Pmmn$ (No 47), with a two-fold rotation axis. Finally, asymmetric slabs with perfect Sr_2O and SrSn surfaces will correspond to a $P4mm$ (No 99) space group, which does not possess either the spacial inversion symmetry nor the mirror symmetry. As already said, this lack of inversion symmetry, which would exist for real surfaces, allows the apparition of an internal electric field, but also of Rashba-like spin splittings in the band structure. Looking at the fine details of the band structures of Fig. 12, we can indeed notice many lifts of degeneracy, which can be associated with Rashba-like spin splittings, as it was shown in Figs. 3 and 6. We can see from these figures that the spin component is null in directions parallel to the wavevector \mathbf{k} and we also found it is zero in the $z[001]$ direction, which is the polar axis (*i.e.* the normal to the surface): These features are characteristics of the Rashba effect. To characterize the energy spin splitting in a simple manner (without considering the point group),

TABLE II. Effective masses m^* and spin splitting parameters a and b calculated for the bands of energy E , the closest from the Fermi level at the X and M points.

Direction	$E - E_F$ (eV)	m^* (m_0)	a (eV Å)	b (eV Å 3)
Sr ₂ O termination				
X → Γ	0.042	-0.54	0.10	-2.2
X → M	0.042	1.34	0.16	-1.6
M → X	0.606	-0.23	0.07	0
M → Γ	0.606	-0.33	0.08	-0.33
SrSn termination				
X → Γ	-0.077	4.04	0.04	0.47
X → M	-0.077	-2.03	0.21	-1.68
M → X	0.204	-0.69	0.05	-1.42
M → Γ	0.204	-0.88	0.05	-2.48

it is possible to fit the difference between the energy of the two bands of opposite spin ΔE_{\pm} as a function of the wavevector k by a third order polynom, such as $\Delta E_{\pm}(k) = a \cdot k + b \cdot k^3$ [63]. Around the M point of little point group C_{4v} , the coefficient a corresponds to the linear Rashba coefficient multiplied by a factor 2 and the cubic term b can be decomposed into two terms [namely γ' and γ'' in Ref. [64]]. The spin-splitting values fitted from our calculations around the X and M high-symmetry points are summarized in Table II. If the values of each coefficient remain modest, it can be noticed from the band structures that the spin splittings are enhanced in the vicinity of band anti-crossings. Interesting spin splittings can also be noticed near the Γ point, but due to the higher number of bands, mixing surface and bulk states, their analysis is more complex.

Appendix C: Effect of the spin-orbit interaction

In this section, we provide the band structures calculated for the two perfect surface terminations without the spin-orbit interaction; the band structures of Fig. 14 can be compared with those of Figs. 2(a) and 5(a) to understand the effect of this interaction.

Appendix D: Surface formation energy

The method used to calculate the surface formation energy [65, 66] consists in

- defining the chemical potentials ranges for which the considered bulk compound is stable, in regard to all the other possible competitive phases,
- searching for the most stable (001) surface terminations in the bulk stability range of chemical potentials, by comparing the enthalpies of formation.

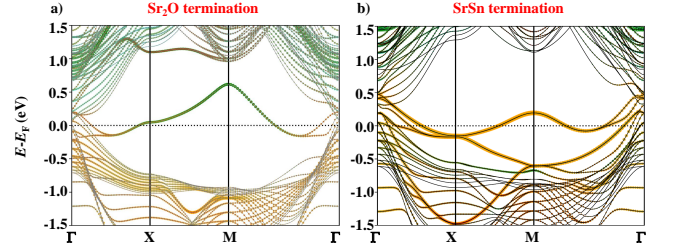


FIG. 14. Band structure calculated without the spin-orbit interaction for the (a) Sr₂O-terminated and (b) SrSn-terminated surface. The same color code is applied as in Fig. 2.

This method is explained in the following for a general X_3YZ perovskite compound and then applied in the specific case of Sr₃SnO.

1. Enthalpy of formation of bulk Sr₃SnO antiperovskite

The enthalpy of formation $\Delta_f H$ of an antiperovskite of formula X_3YZ can be expressed as:

$$\Delta_f H(X_3YZ) = E_{X_3YZ}^{\text{bulk}} - \sum_i N_i E_i^{\text{bulk/gas}} \quad (\text{D1})$$

where $E_{X_3YZ}^{\text{bulk}}$ is the ground state total energy calculated for the X_2YZ antiperovskite, $E_i^{\text{bulk/gas}}$ are the total energies of the X, Y and Z atoms in their pure solid or gas phase and N_i are the number of atoms of each chemical specy. In the antiperovskite compound, the chemical potentials μ_i of these atoms may differ from $E_i^{\text{bulk/gas}}$ by an energy $\Delta\mu_i$, i.e. $\mu_i = E_i^{\text{bulk/gas}} + \Delta\mu_i$.

The conditions for the bulk antiperovskite to be stable are given by the following identity:

$$3\Delta\mu_X + \Delta\mu_Y + \Delta\mu_Z = \Delta_f H_B(X_3YZ) \quad (\text{D2})$$

with $\Delta_f H_B$ the formation enthalpy of the bulk antiperovskite, and by the following equations, which need to be verified in order to avoid any competitive phase to form:

$$n_x \Delta\mu_X + n_y \Delta\mu_Y + n_z \Delta\mu_Z \leq \Delta_f H_B(X_x Y_y Z_z) \quad (\text{D3})$$

It is then possible to calculate a phase diagram, as proposed in Fig. 15, in which we can identify the couple of values of $(\Delta\mu_{Y=\text{Sn}}, \Delta\mu_{X=\text{Sr}})$ for which Sr₃SnO can be formed. In particular, knowing $\Delta_f H(\text{Sr}_3\text{SnO})$ from Eq. D1, it is possible to notice that $\Delta\mu_O$ is always bound to $\Delta\mu_{\text{Sr}}$ and $\Delta\mu_{\text{Sn}}$ through the relation of Eq. D2. Moreover, the variation of chemical potential of the oxygen atoms $\Delta\mu_O$ can be related to the experimental growth conditions, i.e. the temperature T and the pressure P , using thermodynamical models as proposed in Refs. [66] and [67].

A first list of competitive phases has been established thanks to the *Materials project* database [68]; when several stable structures were reported for a given chemical composition, we selected the most stable one after a structural optimization performed keeping the same calculation parameters. The space groups are computed using the *FINDSYM* program [69, 70] with a tolerance of 10^{-3} Å applied on the atom coordinates and lattice parameters.

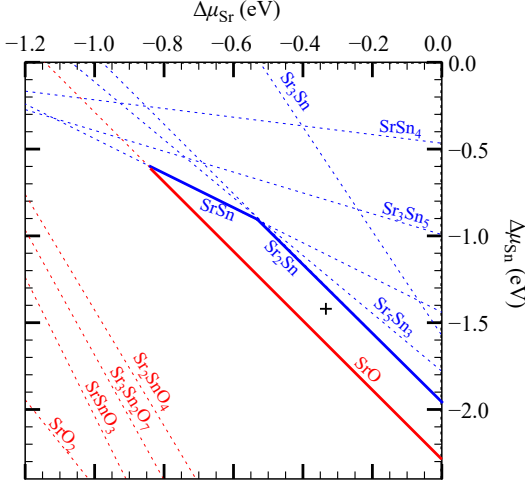


FIG. 15. Stability phase diagram of bulk Sr_3SnO oxide. Red and blue lines correspond to the constrain given by Eq. D3, blue and red colors means that Sr_3SnO is stable respectively below or above the given limit. This allows to define the stability domain delimited by the solid lines.

1127

2. Surface energy

1128 Considering a slab formed by a symmetric layer with
1129 two identical surfaces, we express the surface energy γ_S :

$$\gamma_S = \frac{1}{2A} \left[E_S - \sum_i N_i \mu_i \right] \quad (D4)$$

1130 with E_S the total energy of the slab of X_3YZ comporting
1131 two identical surfaces S of termination i and of area A .
1132 The chemical potentials μ_i are those calculated in the
1133 previous step, such as they are at equilibrium with the
1134 bulk.

1135 It is also convenient to reformulate Eq. D4 explicitly
1136 as a function of $(\Delta\mu_{Y=\text{Sn}}, \Delta\mu_{X=\text{Sr}})$, which for the study
1137 of Sr_3SnO surfaces gives:

$$\gamma_S = \frac{1}{2A} [\alpha + \beta\Delta\mu_{\text{Sr}} + \zeta\Delta\mu_{\text{Sn}}]$$

with

$$\alpha = E_S - \sum_{i=\text{Sr},\text{Sn},\text{O}} N_i E(i) - N_{\text{O}} \Delta_f H_{\text{B}} (\text{Sr}_3\text{SnO}) \quad (D5)$$

$$\beta = 3N_{\text{O}} - N_{\text{Sr}}$$

$$\zeta = N_{\text{O}} - N_{\text{Sn}}$$

1138 By comparing the surface energy γ_S calculated for
1139 different surface terminations, it is possible to determine
1140 which atomic structure is the most stable for a selected
1141 couple of values $(\Delta\mu_{Y=\text{Sn}}, \Delta\mu_{X=\text{Sr}})$; interesting couples
1142 of values will be in particular those for which bulk Sr_3SnO
1143 is stable.

1144 As mentioned in Refs. [71–73], calculating surface
1145 energies of polar oxides requires a lot of care and it is
1146 important to verify the convergence as a function of the
1147 vacuum and film thicknesses and of the k mesh used
1148 for the first Brillouin zone sampling, in order to ensure
1149 a good convergence of the energy as a function of the
1150 slab thickness (the reader can refer to Ref. [73] for more
1151 information about the different methods to circumvent
1152 such a problem). Performing our calculations, we
1153 verified that the 2D k -mesh sampling used for the
1154 (001) slabs was matching with those used for the bulk
1155 calculations and we also checked that, by varying the slab
1156 thickness, we have a precision of 5 meV on the surface
1157 energy. Another critical point, which is standard in
1158 DFT calculations, arises from the choice of the exchange-
1159 correlation functional. In particular, it has been pointed
1160 out that the binding energy of the O_2 molecule may be
1161 overestimated [71, 72], which would justify the need to
1162 correct the chemical potential of oxygen atoms by shifting
1163 its value. If applying such correction would change the
1164 calculated formation energies of Sr_3SnO , the chemical
1165 potential of the oxygen atoms does not appear in the
1166 equation D5. Since different surface energies can display
1167 very close surface energies, depending on the growth
1168 conditions, we can in any case expect that different
1169 terminations will be present in real samples, explaining
1170 why we decided to compare different terminations.

3. Energy of defect formation

1172 Another way to describe the previously mentioned
1173 surface terminations is to consider that they correspond
1174 to the association of a perfect surface termination with
1175 point defects. It is thus possible to define an energy of
1176 formation of the defect, which is expressed as a function
1177 of the energy of the slab or bulk supercell:

$$E_d = E_{\text{sd}} - \left(E_{\text{sp}} + \sum_i N_i \mu_i \right) \quad (D6)$$

TABLE III. Formation energies of defects E_d calculated using the values: $\Delta\mu_{\text{Sr}} = -0.341$ eV, $\Delta\mu_{\text{Sn}} = -1.440$ eV and $\Delta\mu_{\text{O}} = -5.484$ eV. For information, we also provide the averaged Sn-3d CLSs calculated with the $3 \times 3 \times 3$ supercells.

Surface dimension	Type of defect	E_d (eV/defect)	$\langle\Delta\varepsilon_{\text{Sn},3d}\rangle$ (eV)
Bulk			
$(2 \times 2 \times 2)$	V_{Sr}	0.22	
$(3 \times 3 \times 3)$	V_{Sr}	0.05	0.359
$(2 \times 2 \times 2)$	V_{Sn} (NM)	0.32	
$(3 \times 3 \times 3)$	V_{Sn}	0.09	-0.276
$(4 \times 4 \times 4)$	V_{Sn}	0.04	
$(2 \times 2 \times 2)$	V_{O}	0.15	
$(3 \times 3 \times 3)$	V_{O}	0.05	-0.066

with E_{sd} and E_{sp} the energies of the supercell respectively with and without the defect, and $\mu_i = E_i^{\text{bulk/gas}} + \Delta\mu_i$. With this new equation again, the formation energy E_d depends on the chosen values of the chemical potentials; taking the same averaged values as previously, we can then obtain the formation energies given in Table III and IV.

a. Formation of point defects in the bulk compound: We calculated the effect of vacancies in bulk supercells. The energies of formation, summarized in Table III, show that it is difficult to calculate an accurate energy for individual defects and that they strongly depend on the supercell size.

As calculated previously by Batool *et al.* [30], we found that a Sn vacancy induces the appearance of a ferromagnetic ordering by populating Sr-4d bands: We calculated a total magnetic moment of $1.04 \mu_B$, which is comparable to the value of $1.28 \mu_B$ given in Ref. [30] and to the value calculated for the surface, *i.e.* $0.84 \mu_B$. This magnetic ordering is weak and is likely to be destroyed by the addition of defects at the surface. In the case of the bulk calculations, we found that it only appears for a very high content of vacancies, that is for the smallest supercell with $2 \times 2 \times 2$ dimensions.

b. Formation of defects at the surface: As seen in the previous paragraph, speaking of formation energy of a defect is not rigorous because of the high given in Fig. 16.

content of defects we considered; the concept of surface reconstruction is more adapted to this study. The formation energies given in Table IV, however, allows us to have an idea of the energy difference separating the different surface terminations for a given set of chemical potentials.

For the Sr_2O termination, we tested two different latteral dimensions to build our slabs: $(\sqrt{2} \times \sqrt{2})\text{R}45^\circ$ and (2×1) . We can notice that the latter one gives almost systematically lower formation energies than the first one, which means that the (2×1) geometry gives more stable structures when including defects. This explains

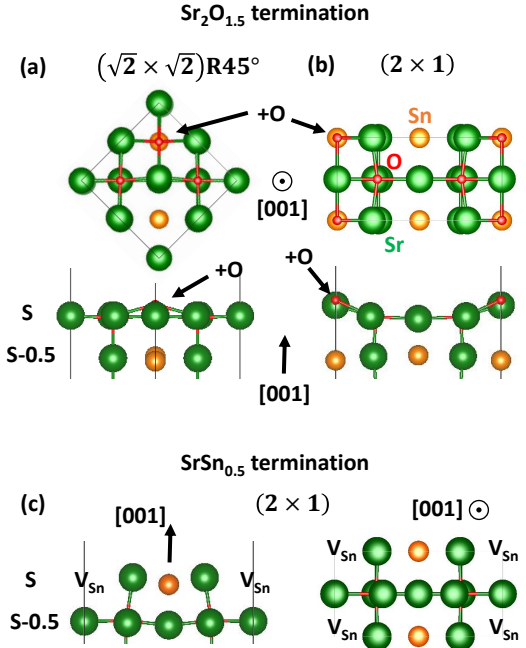


FIG. 16. Optimized atomic structure (side and top view) of the defective surface: (a) and (b) represent respectively the $(\sqrt{2} \times \sqrt{2})\text{R}45^\circ$ and (2×1) $\text{Sr}_2\text{O}_{1.5}$ surfaces, *i.e.* surfaces with a Sr_2O termination and an additional oxygen atom located in an interstitial position of the surface layer (S), (on top of a Sn atom from the subsurface layer (S-0.5)); (c) corresponds to a (2×1) SrSn surface with a Sn vacancy.

why we only discuss this configuration in the main text. Examples of relaxed structures calculated for the oxygen-rich Sr_2O surface and for the Sn-deficient SrSn surface are given in Fig. 16.

-
- [1] S. V. Krivovichev, Z. Kristallogr. **223**, 109 (2008).
[2] J. Mannhart and D. G. Schlom, Science **327**, 1607 (2010).
[3] H. Y. Hwang, Y. Iwasa, M. Kawasaki, B. Keimer, and Y. Nagaosa, Nature Mater. **11**, 103 (2012).
[4] The interface is still the device, Nature Mater. **11**, 10.1038/nmat3244.
[5] M. Bilal, S. Jalali-Asadabadi, R. Ahmad, and I. Ahmad, J. Chem. **2015**, 495131 (2015).
[6] Y. Wang, H. Zhang, J. Zhu, X. Lü, S. Li, R. Zou, and Y. Zhao, Adv. Mater. **32**, 1905007 (2020).
[7] T. He, Q. Huang, A. P. Ramirez, Y. Wang, K. A. Regan, N. Rogado, M. A. Hayward, M. K. Haas, J. S. Slusky, K. Inumara, H. W. Zandbergen, N. P. Ong, and R. J.

TABLE IV. Formation energies of defects E_d at the $\text{Sr}_3\text{SnO}(001)$ surfaces. The calculations have been performed using Eq. D6 and with the variations of chemical potentials corresponding to the middle of the Sr_3SnO stability domain given by the black cross in Fig. 15, *i.e.* $\Delta\mu_{\text{Sr}} = -0.341$ eV, $\Delta\mu_{\text{Sn}} = -1.440$ eV and $\Delta\mu_{\text{O}} = -5.484$ eV. The defect "+O" corresponds to an oxygen adatom located either in the surface layer (S) on top of the subsurface Sn atom, or initially on top (S+1) of a surface Sr atom. For the (2×1) , there are two non-equivalent Sr atom (labeled "1" and "2"), which are respectively aligned with the oxygen atoms along the [010] and [100] directions (the [010] direction being twice shorter than the [100] direction, this may explain why the Sr1 vacancy is less stable than the Sr2 vacancy).

Surface dimension	Type of defect	location	E_d
			(eV/defect)
SrO ₂ termination			
$(\sqrt{2} \times \sqrt{2})\text{R}45^\circ$	V _{Sr}	S	0.60
$(\sqrt{2} \times \sqrt{2})\text{R}45^\circ$	V _{Sr}	S-0.5	1.28
$(\sqrt{2} \times \sqrt{2})\text{R}45^\circ$	V _{Sn}	S-0.5	1.88
$(\sqrt{2} \times \sqrt{2})\text{R}45^\circ$	V _O	S	0.61
$(\sqrt{2} \times \sqrt{2})\text{R}45^\circ$	+O	S	0.40
$(\sqrt{2} \times \sqrt{2})\text{R}45^\circ$	+O	S+1	4.14
(2×1)	V _{Sr1}	S	1.00
(2×1)	V _{Sr2}	S	0.40
(2×1)	V _{Sr}	S-0.5	0.99
(2×1)	V _{Sn}	S-0.5	1.77
(2×1)	V _O	S	0.54
(2×1)	+O	S	0.25
SrSn termination			
(2×1)	V _{Sr}	S	2.09
(2×1)	V _{Sr1}	S-0.5	2.32
(2×1)	V _{Sr2}	S-0.5	1.84
(2×1)	V _{Sn}	S	-0.21
(2×1)	V _O	S-0.5	0.42

- 1235 Cava, Nature **411**, 54 (2001).
1236 [8] Y. Sun, X.-Q. Chen, S. Yunoki, D. Li, and Y. Li, Phys. Rev. Lett. **105**, 216406 (2010).
1237 [9] R. Yu, H. Weng, Z. Fang, X. Dai, and X. Hu, Phys. Rev. Lett. **115**, 036807 (2015).
1238 [10] W. F. Goh and W. E. Pickett, Phys. Rev. B **97**, 035202 (2018).
1239 [11] C. X. Quintela, K. Song, D.-F. Shao, L. Xie, T. Nan, T. R. Paudel, N. Campbell, X. Pan, T. Tybell, M. S. Rzchowski, E. Y. Tsymbal, S.-Y. Choi, and C.-B. Eom, Sci. Adv. **6**, 10.1126/sciadv.aba4017 (2020).
1240 [12] A. Widera and H. Schäfer, Mater. Res. Bull. **15**, 1805 (1980).
1241 [13] H. Nakamura, D. Huang, J. Merz, E. Khalaf, P. Ostrovsky, A. Yaresko, D. Samal, and H. Takagi, Nature Commun. **11**, 1161 (2020).
1242 [14] T. H. Hsieh, J. Liu, and L. Fu, Phys. Rev. B **90**, 081112 (2014).
1243 [15] C.-K. Chiu, Y.-H. Chan, X. Li, Y. Nohara, and A. P. Schnyder, Phys. Rev. B **95**, 035151 (2017).
1244 [16] L. Fu, Phys. Rev. Lett. **106**, 106802 (2011).
1245 [17] Y. Fang and J. Cano, Phys. Rev. B **101**, 245110 (2020).
1246 [18] M. Oudah, A. Ikeda, J. N. Hausmann, S. Yonezawa, T. Fukumoto, S. Kobayashi, M. Sato, and Y. Maeno, Nature Commun. **7**, 13617 (2016).
1247 [19] J. N. Hausmann, M. Oudah, A. Ikeda, S. Yonezawa, and Y. Maeno, Supercond. Sci. Technol. **31**, 055012 (2018).
1248 [20] M. Oudah, J. N. Hausmann, S. Kitao, A. Ikeda, S. Yonezawa, M. Seto, and Y. Maeno, Sci. Rep. **9**, 1831 (2019).
1249 [21] Y. F. Lee, F. Wu, R. Kumar, F. Hunte, J. Schwartz, and J. Narayan, Appl. Phys. Lett. **103**, 112101 (2013).
1250 [22] D. Huang, H. Nakamura, K. Küster, A. Yaresko, D. Samal, N. B. M. Schröter, V. N. Strocov, U. Starke, and H. Takagi, Phys. Rev. Materials **3**, 124203 (2019).
1251 [23] M. Minohara, R. Yukawa, M. Kitamura, R. Kumai, Y. Murakami, and H. Kumigashira, J. Cryst. Growth **500**, 33 (2018).
1252 [24] P. W. Tasker, J. Phys. C: Solid State Phys. **12**, 4977 (1979).
1253 [25] J. Goniakowski, F. Finocchi, and C. Noguera, Rep. Prog. Phys. **71**, 016501 (2007).
1254 [26] A. Ohtomo and H. Y. Hwang, Nature **427**, 423 (2004).
1255 [27] A. Savoia, D. Paparo, P. Perna, Z. Ristic, M. Salluzzo, F. Miletto Granozio, U. Scotti di Uccio, C. Richter, S. Thiel, J. Mannhart, and L. Marrucci, Phys. Rev. B **80**, 075110 (2009).
1256 [28] D. Samal, H. Nakamura, and H. Takagi, APL Mater. **4**, 076101 (2016).
1257 [29] Y. Ma, A. Edgeton, H. Paik, B. D. Faeth, C. T. Parzyck, B. Pamuk, S.-L. Shang, Z.-K. Liu, K. M. Shen, D. G. Schlom, and C.-B. Eom, Adv. Mater. **32**, 2000809 (2020).
1258 [30] J. Batool, S. M. Alay-e Abbas, A. Ali, K. Mahmood, S. Akhtar, and N. Amin, RSC Adv. **7**, 6880 (2017).
1259 [31] M. Bilal, S. M. A. e Abbas, A. Laref, M. Noor, and N. Amin, J. Phys. Chem. Solids **136**, 109191 (2020).
1260 [32] G. Kresse and J. Hafner, Phys. Rev. B **49**, 14251 (1994).
1261 [33] G. Kresse and J. Furthmüller, Phys. Rev. B **54**, 11169 (1996).
1262 [34] P. E. Blöchl, Phys. Rev. B **50**, 17953 (1994).
1263 [35] G. I. Csonka, J. P. Perdew, A. Ruzsinszky, P. H. T. Philipsen, S. Lebègue, J. Paier, O. A. Vydrov, and J. G. Ángyán, Phys. Rev. B **79**, 155107 (2009).
1264 [36] H. J. Monkhorst and J. D. Pack, Phys. Rev. B **13**, 5188 (1976).
1265 [37] W. Tang, E. Sanville, and G. Henkelman, J. Phys. Condens. Matter **21**, 084204 (2009).
1266 [38] T. Kariyado and M. Ogata, Journal of the Physical Society of Japan **80**, 083704 (2011).
1267 [39] T. Kariyado and M. Ogata, J. Phys. Soc. Jpn. **81**, 064701 (2012).
1268 [40] A. Walsh, A. A. Sokol, J. Buckeridge, D. O. Scanlon, and C. R. A. Catlow, Nature Mater. **17**, 958 (2018).
1269 [41] W. Egelhoff, Surf. Sci. Rep. **6**, 253 (1987).
1270 [42] M. Methfessel, D. Hennig, and M. Scheffler, Surf. Sci. **287-288**, 785 (1993), proceedings of the 8th International Conference on Solid Surfaces.
1271 [43] W. Olovsson, C. Göransson, T. Marten, and I. A. Abrikosov, Phys. Status Solidi (b) **243**, 2447 (2006).
1272 [44] A. Brinkman, M. Huijben, M. van Zalk, J. Huijben, U. Zeitler, J. C. Maan, W. G. van der Wiel, G. Rijnders, D. H. A. Blank, and H. Hilgenkamp, Nature Mater. **6**, 493 (2007).
1273 [45] N. Pavlenko, T. Kopp, E. Y. Tsymbal, G. A. Sawatzky,

- 1319 and J. Mannhart, Phys. Rev. B **85**, 020407 (2012).
 1320 [46] L. Yu and A. Zunger, Nature Commun. **5**, 5118 (2014).
 1321 [47] B. Kalisky, J. A. Bert, B. B. Klopfer, C. Bell, H. K. Sato,
 1322 M. Hosoda, Y. Hikita, H. Y. Hwang, and K. A. Moler,
 1323 Nature Commun. **3**, 922 (2012).
 1324 [48] B. Santara, P. K. Giri, K. Imakita, and M. Fujii,
 1325 Nanoscale **5**, 5476 (2013).
 1326 [49] N. H. Hong, J. Sakai, N. Poirot, and V. Brizé, Phys. Rev.
 1327 B **73**, 132404 (2006).
 1328 [50] G. Bouzerar and T. Ziman, Phys. Rev. Lett. **96**, 207602
 1329 (2006).
 1330 [51] N. H. Hong, N. Poirot, and J. Sakai, Phys. Rev. B **77**,
 1331 033205 (2008).
 1332 [52] S. Ning, P. Zhan, Q. Xie, Z. Li, and Z. Zhang, J. Phys.
 1333 D: Appl. Phys. **46**, 445004 (2013).
 1334 [53] J. Berashevich and A. Reznik, Journal of Physics and
 1335 Chemistry of Solids **75**, 1132 (2014).
 1336 [54] M. A. Rahman, S. Rout, J. P. Thomas, D. McGillivray,
 1337 and K. T. Leung, J. Am. Chem. Soc. **138**, 11896 (2016).
 1338 [55] E. Albanese, A. Ruiz Puigdollers, and G. Pacchioni, ACS
 1339 Omega **3**, 5301 (2018).
 1340 [56] K. Kalam, H. Seemen, M. Mikkor, P. Ritslaid, R. Stern,
 1341 S. Dueñas, H. Castán, A. Tamm, and K. Kukli, ECS
 1342 Journal of Solid State Science and Technology **7**, N117
 1343 (2018).
 1344 [57] M. Venkatesan, C. B. Fitzgerald, and J. M. D. Coey,
 1345 Nature **430**, 630 (2004).
 1346 [58] J. Vidal, X. Zhang, L. Yu, J.-W. Luo, and A. Zunger,
 1347 Phys. Rev. B **84**, 041109 (2011).
 1348 [59] J. Sun, A. Ruzsinszky, and J. P. Perdew, Phys. Rev. Lett.
 1349 **115**, 036402 (2015).
 1350 [60] S. L. Dudarev, G. A. Botton, S. Y. Savrasov, C. J.
 1351 Humphreys, and A. P. Sutton, Phys. Rev. B **57**, 1505
 1352 (1998).
 1353 [61] J. Heyd, G. E. Scuseria, and M. Ernzerhof, J. Chem.
 1354 Phys. **124**, 219906 (2006).
 1355 [62] M. Stengel, Phys. Rev. Lett. **106**, 136803 (2011).
 1356 [63] J. Gosteau, R. Arras, P. Chen, H. J. Zhao, C. Paillard,
 1357 and L. Bellaiche, Phys. Rev. B **103**, 024416 (2021).
 1358 [64] R. Arras, J. Gosteau, H. J. Zhao, C. Paillard, Y. Yang,
 1359 and L. Bellaiche, Phys. Rev. B **100**, 174415 (2019).
 1360 [65] K. Reuter and M. Scheffler, Phys. Rev. B **65**, 035406
 1361 (2001).
 1362 [66] E. Heifets, E. A. Kotomin, Y. A. Mastrikov, S. Piskunov,
 1363 and J. Maier, Thermodynamics - interaction studies
 1364 - solids, liquids and gases (InTech, 2011) Chap.
 1365 19.Thermodynamics of ABO_3 -type perovskite surfaces.
 1366 [67] J. Osorio-Guillén, S. Lany, S. V. Barabash, and
 1367 A. Zunger, Phys. Rev. Lett. **96**, 107203 (2006).
 1368 [68] A. Jain, S. P. Ong, G. Hautier, W. Chen, W. D. Richards,
 1369 S. Dacek, S. Cholia, D. Gunter, D. Skinner, G. Ceder,
 1370 and K. A. Persson, APL Mater. **1**, 011002 (2013).
 1371 [69] H. T. Stokes and D. M. Hatch, J. Appl. Crystallogr. **38**,
 1372 237 (2005).
 1373 [70] H. T. Stokes, D. M. Hatch, and B. J. Campbell.,
 1374 FINDSYM, ISOTROPY Software Suite, iso.byu.edu
 1375 (2005).
 1376 [71] L. Wang, T. Maxisch, and G. Ceder, Phys. Rev. B **73**,
 1377 195107 (2006).
 1378 [72] D. Kramer and G. Ceder, Chem. Mater. **21**, 3799 (2009).
 1379 [73] W. Sun and G. Ceder, Surf. Sci. **617**, 53 (2013).